The Astrophysical Journal, 939:117 (23pp), 2022 November 10 https://doi.org/10.3847/1538-4357/ac966f

New Identifications and Multiwavelength Properties of Extragalactic Fermi Gamma-Ray Sources in the SPT-SZ Survey Field

Lizhong Zhang (张力中)[1,2,3], Joaquin D. Vieira[2,3,4], Marco Ajello[5], Matthew A. Malkan[6], Melanie A. Archipley[3,4], Joseph Capota[2], Allen Foster[7], and Greg Madejski[8]

[1] Department of Physics, University of California, Santa Barbara, CA 93106, USA; lizhong4physics@gmail.com
[2] Department of Physics, University of Illinois at Urbana-Champaign, 1110 West Green St, Urbana, IL 61801, USA
[3] Department of Astronomy, University of Illinois at Urbana-Champaign, 1002 West Green St, Urbana, IL 61801, USA
[4] Center for AstroPhysical Surveys, National Center for Supercomputing Applications, Urbana, IL 61801, USA
[5] Department of Physics and Astronomy, Clemson University, 118 Kinard Laboratory, Clemson, SC 29631, USA
[6] Department of Physics and Astronomy, University of California, Los Angeles, 475 Portola Plaza, Los Angeles, CA 90095-1547, USA
[7] Department of Physics, Case Western Reserve University, Cleveland, OH 44106, USA
[8] Kavli Institute for Particle Astrophysics and Cosmology, Department of Physics and SLAC National Accelerator Laboratory, Stanford University, Stanford, CA 94305, USA

Received 2022 July 20; revised 2022 September 18; accepted 2022 September 28; published 2022 November 14

Abstract

The fourth Fermi Large Area Telescope catalog (4FGL) contains 5064 γ-ray sources detected at high significance, but 26% of them still lack associations at other wavelengths. The SPT-SZ survey, conducted between 2008 and 2011 with the South Pole Telescope (SPT), covers 2500 deg^2 of the southern sky in three millimeter-wavelength (mm) bands and was used to construct a catalog of nearly 5000 emissive sources. In this study, we introduce a new cross-matching scheme to search for multiwavelength counterparts of extragalactic γ-ray sources using a mm catalog. We apply a Poissonian probability to evaluate the rate of spurious false associations and compare the multiwavelength associations from the radio, mm, near-infrared, and X-ray with 4FGL γ-ray sources. In the SPT-SZ survey field, 85% of 4FGL sources are associated with mm counterparts. These mm sources include 94% of previously associated 4FGL sources and 56% of previously unassociated 4FGL sources. The latter group contains 40 4FGL sources for which SPT has provided the first identified counterparts. Nearly all of the SPT-associated 4FGL sources can be described as flat-spectrum radio quasars or blazars. We find that the mm band is the most efficient wavelength for detecting γ-ray blazars when considering both completeness and purity. We also demonstrate that the mm band correlates better to the γ-ray band than the radio or X-ray bands. With the next generation of CMB experiments, this technique can be extended to greater sensitivities and more sky area to further complete the identifications of the remaining unknown γ-ray blazars.

Unified Astronomy Thesaurus concepts: Active galactic nuclei (16); Blazars (164); Gamma-ray sources (633); Radio loud quasars (1349); Relativistic jets (1390); Submillimeter astronomy (1647)

Supporting material: figure set, machine-readable tables

1. Introduction

The γ-ray background holds important clues to the nature of galaxy evolution, the cosmic history of black hole accretion, and possibly the nature of dark matter (Ajello et al. 2015; Funk 2015). Unveiling the nature of the unassociated Fermi Large Area Telescope (LAT) sources is one of the biggest challenges in γ-ray astronomy, due to the relatively large point-spread function, and is necessary to understand the contribution of various source classes to the γ-ray background.

Blazars are a subclass of active galactic nuclei (AGN) with relativistic jets of high-energy particles pointing near our line of sight (e.g., Urry & Padovani 1995). Their nonthermal emission is generally detected across the entire electromagnetic spectrum from radio to γ-ray bands. Blazars are subclassified into flat-spectrum radio quasars (FSRQs) and BL Lac objects (BL Lacs), according to the equivalent width of the emission lines in their optical spectrum (Stickel et al. 1991; Stocke et al. 1991; Marcha et al. 1996). These two subclasses of blazars are thought to be intrinsically different, perhaps based on their accretion mode (Dermer & Giebels 2016). FSRQs have high luminosity and a thin and radiatively efficient black hole accretion disk (Malkan & Moore 1986), while BL Lacs are powered by an advection-dominated, low radiative efficiency accretion flow (Dermer & Giebels 2016; Blandford et al. 2019). The jet emission is relativistically beamed (Ghisellini 2019), with a Doppler boosting factor corresponding to a bulk Lorentz factor of several to greater than 10 (Pushkarev et al. 2009). In both cases, the broadband spectra consist of two broad humps, one peaking in the IR-to-X-ray regime and the other peaking in the γ-ray regime. The low-energy peak is believed to be due to synchrotron emission, while the high-energy peak is likely due to inverse Compton scattering of low-energy photons of either the same synchrotron photons (for BL Lacs) or external photons from the disk/BLR (for FSRQs) (e.g., Dutka et al. 2017). However, some blazars might not necessarily be detected in γ-rays (e.g., Paliya et al. 2017). Indeed, a recent study showed that blazars undetected in γ-rays are likely to have relatively smaller Doppler factors and more disk dominance (Paliya et al. 2017). In the case of strong Compton scattering, the beaming of γ-rays could be larger than, e.g., that seen in the radio (Dermer 1995), leading to the possible

nondetection (or reduced detection efficiency) of γ-rays from sources not seen exactly pole-on.

The Fermi Gamma-ray Space Telescope has been observing the high-energy sky from 50 MeV to 1 TeV since 2008 (Atwood et al. 2009). The fourth Fermi-LAT catalog (4FGL) of γ-ray sources is based on observations for 8 yr and is a deep all-sky survey in γ-ray bands (Abdollahi et al. 2020). The Fermi 4FGL catalog contains 5064 γ-ray sources detected with at least 4σ significance. More than 62% of these sources are associated with AGNs. Currently, 26% of Fermi 4FGL sources are unassociated. The high Galactic latitude sources may fall in the following categories: blazars, radio galaxies, and millisecond pulsars (e.g., Abdollahi et al. 2020; Schinzel et al. 2017), with the largest fraction of high Galactic latitude (and presumably extragalactic) sources being blazars, where millimeter-wave (mm) emission and γ-ray emission are likely to be produced cospatially in the extremely compact emission regions within the jet (Meyer et al. 2019). This makes the mm regime a very efficient way to identify both blazars and previously unassociated Fermi sources.

Previous studies have targeted monitoring of Fermi γ-ray blazars at various wavelengths, based on, for example, follow-up at radio wavelengths (Schinzel et al. 2015; Schinzel et al. 2017) or the infrared behavior of γ-ray sources with WISE (D'Abrusco et al. 2012; Massaro & D'Abrusco 2016). From these studies, blazars are known to reside at high redshifts ($z > 0.1$) and exhibit extreme apparent luminosities with strong variability.

The South Pole Telescope (SPT; Carlstrom et al. 2011) is a 10 m telescope dedicated to studying the cosmic microwave background (CMB). The SPT has been used to survey thousands of square degrees of the southern extragalactic sky at 1.4, 2.0, and 3 mm with arcminute resolution down to millijansky noise levels. In this work, we focus on the 2500 deg^2 SPT-SZ survey, conducted with the SPT from 2008 to 2011. The SPT-SZ field is at high Galactic latitude ($|b| > 15$), and thus most of the sources are expected to be of extragalactic origin (Everett et al. 2020). Roughly 3500 synchrotron-dominated sources are detected at high significance in the SPT-SZ maps, providing a powerful tool to identify unassociated 4FGL sources. This wavelength regime is particularly suited to uncovering the extragalactic unidentified Fermi 4FGL sources because the mm sources are almost exclusively (>80%) blazars, and blazars are the dominant population in the γ-ray regime. The instrument sensitivity, survey area, and resolution of the SPT are well suited to this task.

In this paper, we establish the methodology of associating mm point sources from CMB surveys with γ-ray sources. In Section 2 we present the data used in this study, while Section 3 describes the association method. Section 4 discusses the implications for the associations, the multiwavelength properties of the new associations, and the comparisons to previous work. In this analysis, we use a flat ΛCDM cosmology with $\Omega_\Lambda = 0.73$, $\Omega_M = 0.27$, and $H_0 = 71$ km s^{-1} Mpc^{-1}.

2. Observational Data

We use multiwavelength data to associate and characterize the 282 4FGL sources within the 2500 deg^2 SPT-SZ survey field (Figure 1). We note that the SPT-SZ field is at high Galactic latitude, and thus it is assumed that the vast majority of the sources are of extragalactic origin. The data sets used in our analysis are summarized below.

2.1. Gamma Rays

We rely on the γ-ray data from the Fermi 4FGL catalog (Abdollahi et al. 2020). We use the source coordinates and 95% uncertainty ellipse for source cross-matching and assume the beam to be Gaussian. The median effective radius for the sources within the 2500 deg^2 SPT-SZ survey field is 3 2. The 0.1–100 GeV energy flux and its uncertainty are used to study the multiwavelength flux correlation and the spectral properties of the associated sources. The class designation in 4FGL is used to evaluate the multiwavelength associations.

2.2. X-Ray

X-ray data are from the ROSAT All-Sky Survey (RASS) Bright Source Catalog (Voges et al. 1999) and the Faint Source Catalog (Voges et al. 2000) at X-ray energies 0.1–2.4 keV. The source coordinates and count rate are both used for 4FGL association. We also use source count rate to analyze potential flux correlation. The statistical signal-to-noise ratio (S/N) reported in the catalog is used when we plot the uncertainties of count rates. Because of the high Galactic latitude of the SPT-SZ field ($|b| > 15$), the soft X-ray ROSAT data are not affected by photoelectric absorption from our own Galaxy. In addition, blazars generally do not exhibit significant intrinsic soft X-ray absorption (Perlman et al. 2005). Therefore, the ROSAT X-ray measurements should be a reliable measure of the X-ray brightness of the blazars, although dependent on the absorption along the line of sight and the different components sampled in blazars of different classes (e.g., synchrotron emission in BL Lacs and inverse Compton emission in FSRQs). However, the X-ray brightness of a blazar may depend on the blazar subclass and which component (synchrotron or inverse Compton scattering) is being sampled by ROSAT.

2.3. Infrared

Infrared data are taken from the Wide-field Infrared Survey Explorer (WISE) AllWISE Source Catalog at 3.4, 4.6, 12, and 22 μm (Wright et al. 2010; Cutri et al. 2013). The angular resolution of WISE ranges from 6″ to 12″ from short to long wavelengths. The source coordinates and flux at 22 μm (W4) are both used for 4FGL association. The flux at 22 μm is also used to study potential flux correlation. The four-band magnitudes are used to perform the WISE color analysis on 4FGL blazars. Both the statistical noise reported in the catalog and an additional 10% uncertainty from calibration in W4 (Wright et al. 2010) are included when we plot the flux uncertainty.

2.4. Millimeter

Millimeter-wave point sources are from the 2500 deg^2 SPT-SZ survey (Everett et al. 2020), which has a spatial resolution of 1.′15 at 150 GHz (2 mm) and an absolute astrometric uncertainty of 2″ (Vieira et al. 2010). The source coordinates and flux at 150 GHz are both used for 4FGL association. The flux at 150 GHz is also used to study the flux correlation and spectral classification. The flux uncertainty includes the statistical noise reported in the catalog, 1.15% uncertainty for the absolute calibration at 150 GHz, and 20% uncertainty from

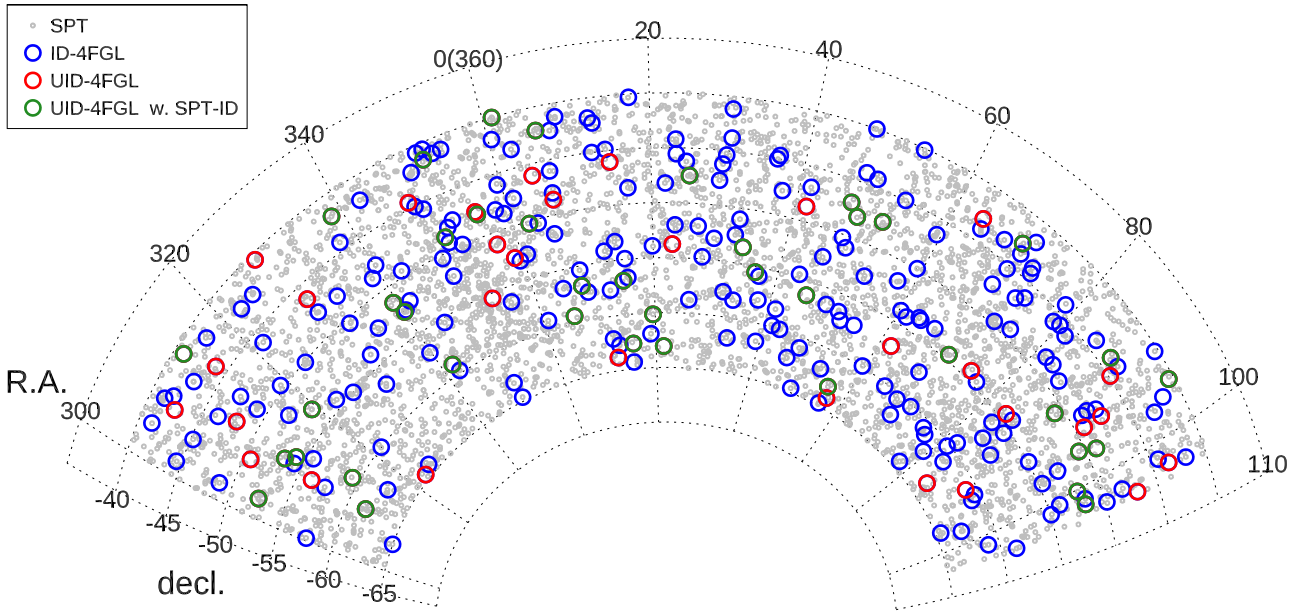

Figure 1. The 2500 deg^2 SPT-SZ survey (Everett et al. 2020). In this region, gray points mark all SPT sources in Everett et al. (2020), green circles represent the position of the previously unassociated 4FGL sources that have SPT counterparts (40), blue circles represent the already-associated 4FGL sources (211), and red circles represent the remaining still-unidentified 4FGL sources (31).

mm source variability. The 20% variability is the median value of the variance in the light curves of the brightest 200 blazars in the SPT-SZ field. The SPT data used in this paper were collected between 2008 and 2011. Note that the published SPT-SZ catalog reaches down to the 4.5σ significance level, but in this work we extended our search down below 4.5σ–1σ using forced photometry directly from the 150 GHz maps using the SUMSS positions as priors. This combination of SUMSS (radio) and SPT (mm) associations will hereafter be referred to as SPT+SUMSS counterparts.

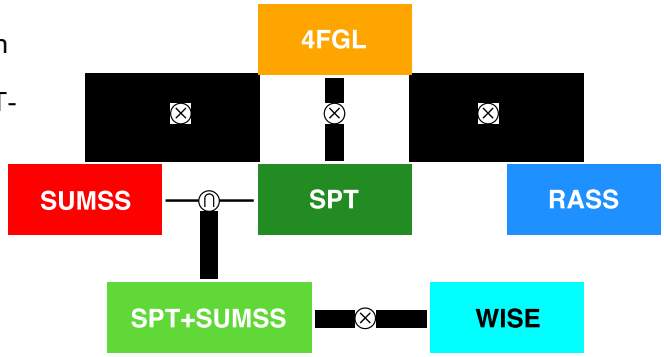

Figure 2. The logic sequence of multiwavelength cross-matching of 4FGL sources. We initially conduct the preliminary 4FGL cross-matching with SUMSS, SPT, and RASS to evaluate the most efficient wavelength for the γ-ray source identification, where the SPT+SUMSS association turns out to maximize the completeness while minimizing the impurity. The true counterparts are selected based on the statistics of the Poissonian probability from the preliminary results. We then take the advantage of mm–radio (SPT+SUMSS) counterparts to refine the position and enable a reliable cross-match with WISE.

2.5. Radio

Radio data are from the Sydney University Molonglo Sky Survey (SUMSS; Mauch et al. 2003) at 843 MHz with 45″ angular resolution and a detection threshold of 6 mJy. The data were taken between 1997 and 2003. The source coordinates and integrated radio flux density are both used for 4FGL association. The flux density is also used to study the flux correlation and spectral classification. In addition to the statistical noise reported in the catalog, we also adopt a 20% uncertainty to account for source variability. This uncertainty is what we observe for sources in the mm on roughly year-long timescales, but note that this is most likely an underestimate for the source variability on the timescales we are comparing fluxes for this work.

2.6. Spectroscopic Redshifts

For each associated 4FGL source, we gather all multi-wavelength data and adopt the most accurate position from the radio/mm/infrared/optical counterpart if available. We obtained spectroscopic redshifts from the NASA/IPAC Extragalactic Database (NED) for any sources for which they were available. Using the archival redshift data, we study the luminosity distribution, multiwavelength flux evolution, and classification distribution of the 4FGL blazars.

3. Method

In this section, we describe the method we use for identifying and associating multiwavelength counterparts with the Fermi 4FGL sources. There are 282 4FGL sources within the 2500 deg^2 SPT-SZ survey field, 71 (25%) of which are previously unassociated with any counterpart. Attempting to cross-match the 4FGL sources to external catalogs by selecting all potential counterparts within a given search radius will often yield multiple potential counterparts, particularly when the external catalog has a high surface number density. There are two quantities associated with every external source that we use for cross-matching. The first is the separation between the potential counterpart and the 4FGL position in units of positional uncertainty (σ_{4FGL}). The second is the probability of false association for a given external source, which is a function of separation, flux density, and catalog density.

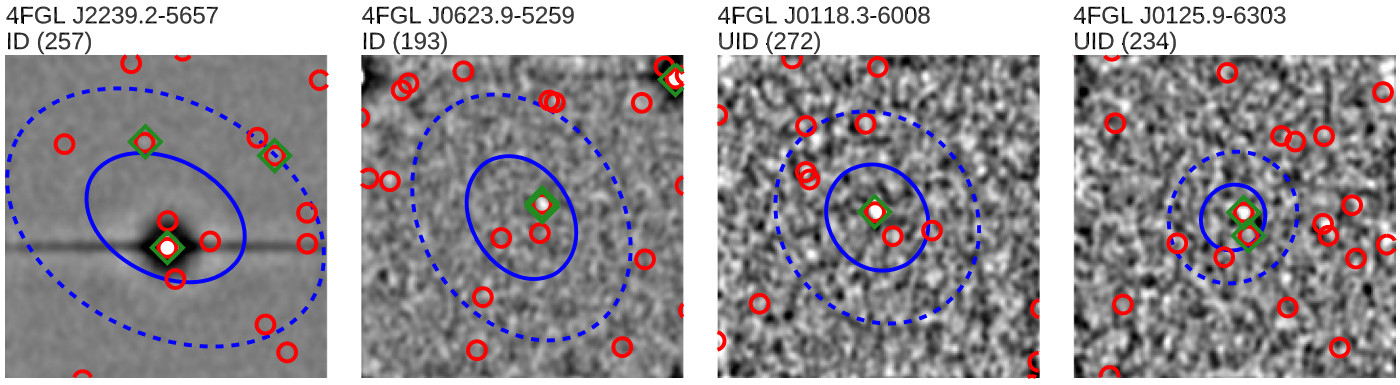

Figure 3. Selected samples illustrating various kinds of 4FGL associations with mm and radio sources. 4FGL source name and thumbnail index (see Appendix A a B for all the sources studied in this work) are shown in the upper left corner of each panel. Each 0°. 7 × 0°. 7 thumbnail in the gray background is the high-pass-filte SPT 150 GHz image. The blue ellipse at the center shows the 4FGL 95% uncertainty position, and the dashed blue ellipse represents the 4σ uncertainty. The gree diamond marks the position of the SPT point source. The red circle shows the position of SUMSS point sources. The first two examples are of previously associate 4FGL sources, which already had known counterparts. In both cases, these known sources are also uniquely identified by SPT (the first is very bright in the mm wa band, while the second is fainter). The last two panels show previously unassociated 4FGL sources. The third panel shows a new unique association with an SPT source. The last panel shows an unusual case where two SPT sources fall within the 4FGL error circle, either or both of which could be producing the γ-ray emissi

In Figure 2, we show the logical flow diagram we use to identify the multiwavelength counterparts, which is described in more detail later in this section. Figure 3 shows the 4FGL positional uncertainty ellipses on top of representative thumbnail images from the SPT-SZ survey and also the positions of radio sources from the SUMSS catalog. (See Appendix C for the thumbnails of the entire sample).

3.1. Probability of False Association

To start our cross-matching analysis, we search for external candidates for each source in the 4FGL catalog within its 4σ positional error ellipse. The choice of 4σ was a qualitative choice, designed to be inclusive of the relatively large positional uncertainties of both Fermi and the external catalogs.

In order to robustly identify the most probable counterpart when there are multiple candidates, and to statistically evaluate the odds of spurious associations, we calculate a simple Poissonian probability (Browne & Cohen 1978; Downes et al. 1986; Biggs et al. 2011), which gives the probability of a matched source being randomly associated within a given area. The Poissonian probability takes into account the angular separation, flux densities, and number density of potential counterparts. The expected number of random associations is

$$m = \pi abn_s(>S), \quad (1)$$

where a and b are semimajor and semiminor axes, respectively, and $n_s(>S)$ is the surface number density of sources brighter than the candidate counterpart. The Poissonian probability (hereafter "p-value") is thus defined as

$$p = 1 - e^{-m}. \quad (2)$$

The p-value constructed in this way is the probability that an association is false, due to spurious coincidence. Thus, if p = 1, the association is highly likely to be real. We note that there are small corrections that can be made to this probability (see, e.g., Downes et al. 1986; Biggs et al. 2011), which we neglect in this work, as the density of sources is relatively low and our sources of interest are rare. In this work, we accept all sources as potential counterparts with p-value < 0.1 within the 4σ association area.

To visualize our cross-matching selection procedure, Figure 4 shows all the sources within 10σ of the 4FGL position with the 4σ 4FGL and p-value < 0.1 cuts indicated by dashed lines. We plot the p-value versus the angular separation in units of positional error (σ_{4FGL}) for each of the external catalogs. In some cases there are multiple counterparts that meet this criterion. When this is the case, we adopt the counterpart with the lowest p-value as the most probable counterpart and show that source in Figure 4 with a black point.

3.2. Completeness and Purity of Individual Catalogs

In Figure 5, we quantify the behavior of the multiwavelength associations in the space of angular separation and the p-value by histograming potential multiwavelength counterparts of 4FGL point sources within their 4σ beam before cutting on p-value.

In the left panel of Figure 5, we show the histogram of angular separation in units of positional error for each of the external catalogs within the adopted cutoff of $4\sigma_{4FGL}$. What is immediately apparent is that the curves are mostly flat above $1\sigma_{4FGL}$ for SUMSS and RASS but peak around $1\sigma_{4FGL}$ for SPT (or SPT+SUMSS), as the separations increase. In the case of SUMSS, the source density is high (~30 sources per square degree), and so there are always potential counterparts to match with, and there are more the farther out you include, and so the problem becomes deciding which is the true counterpart. For RASS, there are simply not many counterparts to match with. SPT (or SPT+SUMSS), however, often has a counterpart to 4FGL, and the density of background sources is low so, the association histogram peaks and then decreases at larger separations.

In the right panel of Figure 5, we plot the histogram of p-value for all sources within the $4\sigma_{4FGL}$ radius. The distribution of SUMSS counterparts is bimodal, with the counterparts split into two groups near 0 and 1, respectively, which indicates that nearly 1/3 of SUMSS sources inside 4σ 4FGL beams are likely to be spurious associations. The SPT (or SPT+SUMSS) and RASS catalogs, however, with much lower densities, have just one peak at low p-value, indicating a high certainty of association.

We adopt the critical p-value (p_{cri}) to best separate the real and false associations. We chose 10% as an acceptable false

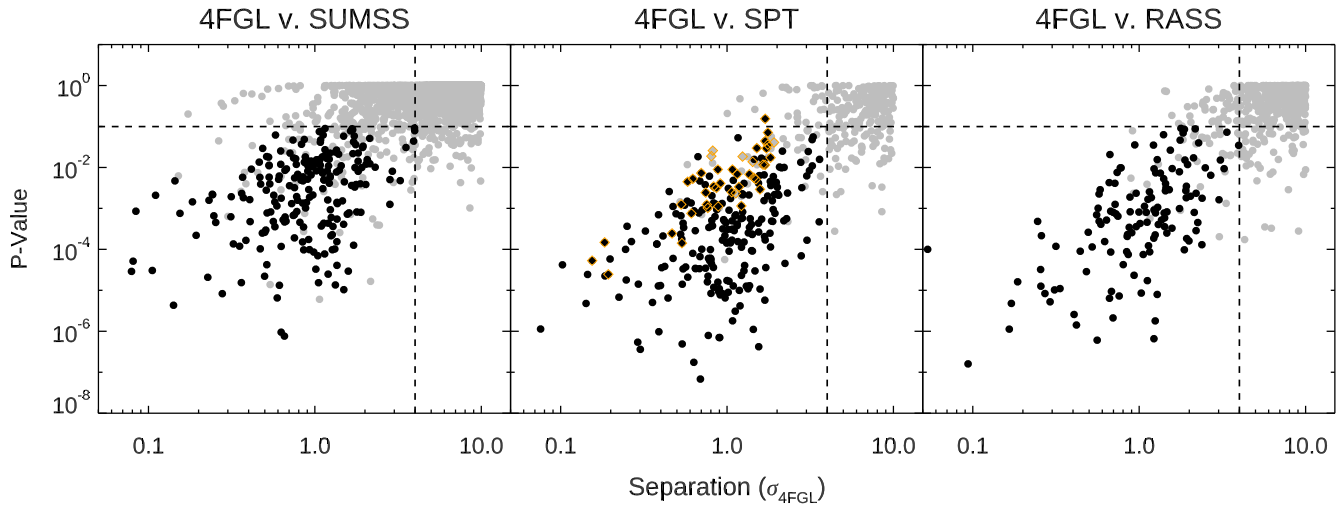

Figure 4. Potential associations of the sources from external catalogs with the 282 4FGL sources in the SPT-SZ survey field plotted with their probability of false association (p-value) vs. source separation in units of positional uncertainty. The gray dots represent all the point sources within 10σ 4FGL positional uncertainty. T vertical and horizontal dashed lines indicate our adopted $r_{<4\sigma_{4FGL}}$ positional separation cut and p-value < 0.1 cut, respectively. The black dots represent the source with the lowest p-value associated with a 4FGL source. Orange diamonds represent faint mm sources with fluxes assigned by forced photometry using positional priors from the SUMSS radio catalog. Note that σ_{4FGL} refers to the standard deviation of the 4FGL position, which varies source by source. Left panel: the SUMSS radio associations are heavily contaminated owing to the excessively high source number density; thus, the region of spurious association extends from the upper region to roughly $4\sigma_{4FGL}$ in separation and 0.1 in probability of false association. Middle panel: the SPT mm association shows more distinct separation between the two groups of the associations in p–r space, while for radio association the contamination of the spurious cross-matching causes the large overlap in the spurious region. With both the high completeness and high purity, mm provides the best combined performance in completeness and reliability. Right panel: the RASS X-ra association shows good purity according to the low probability of false association (most gray dots with $r < 4\sigma_{4FGL}$ have p-value less than 0.1), but the completeness is the lowest compared with the others (see Table 1). Multiwavelength comparisons of sources within $4\sigma_{4FGL}$ in single parameter space are histogrammed in Figure 5. Note that the sources shown at low p-value and separation $< 4\sigma_{4FGL}$, which are shown in gray, are where there are multiple counterparts for a given 4FGL source, and we have adopted the counterpart with the lowest p-value as the association.

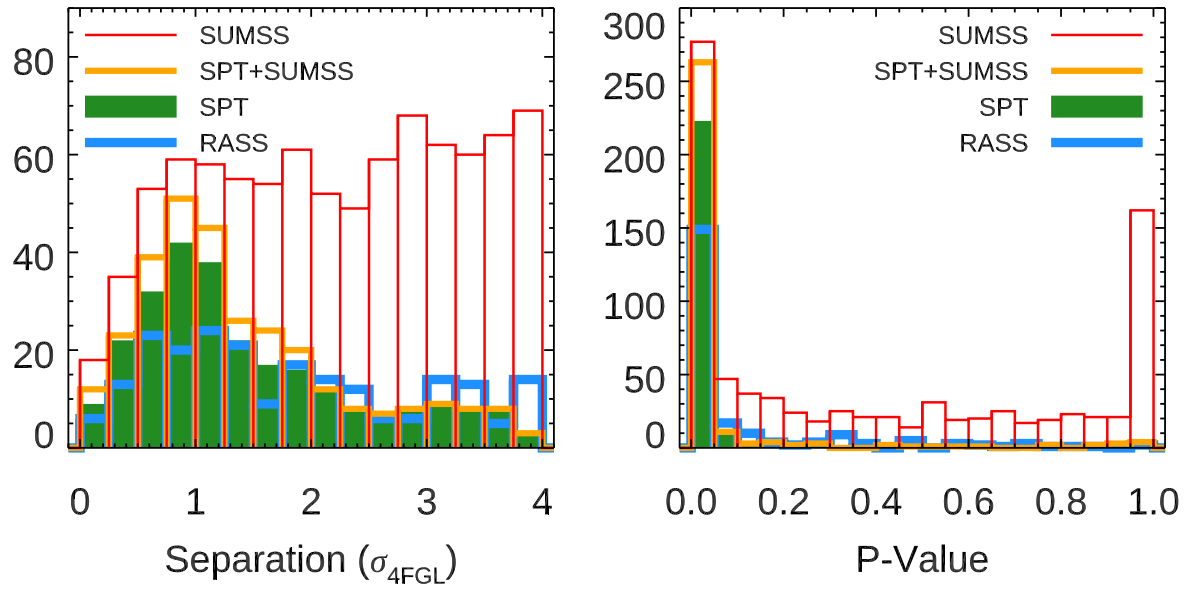

Figure 5. Multiwavelength comparison of the potential associations with 282 4FGL sources in the SPT-SZ survey field. Y-axes for both panels are number of sourc These histograms indicate that SPT+SUMSS is the most efficient identifier of γ-ray counterparts with high completeness and reliability. Left panel: histogram of angular separation of 4FGL sources from SUMSS (radio), SPT (mm), SPT+SUMSS (mm), and RASS (X-ray) positions. The mm and radio associations are highly complete, while X-ray only has around half of their completeness. Right panel: histogram of the probability of false associations of the 4FGL sources with SUMSS, SPT, SPT+SUMSS, and RASS sources. A low probability of false association corresponds to a high certainty of a real counterpart. Thus, the mm and X-ray counterparts are more secure because most of them have the probability of false association less than 0.1, while only around 2/3 radio potential counterparts are within 0.1.

association rate and indicate this cut by the horizontal dashed lines in Figure 4.

For the purpose of defining the efficiency of an external catalog associated with 4FGL sources, we define completeness as the probability of a catalog providing at least one viable counterpart (separation < $4\sigma_{4FGL}$ and p-value > 0.1) to a source in the 4FGL catalog and purity as the probability that the association is false (separation < $4\sigma_{4FGL}$). To calculate the purity of each catalog, we use the equation

$$\text{Purity} = 1 - \frac{1}{N} \sum_{r < 4\sigma_{4FGL}} p, \quad (3)$$

Table 1
Completeness and Purity of 4FGL Multiwavelength Associations within the 2500 deg^2 SPT-SZ Survey Sky

Survey	Σ (deg^{-2})	4FGL (282)	4FGL-ID (211)	4FGL-UID (71)	Completeness (%)	Purity (%)
RASS	3.53	136	119	17	48.2 ± 4.1	89.8 ± 0.23
SPT	1.91	204	181	23	72.3 ± 5.1	93.7 ± 0.01
SPT+SUMSS	1.94	239	199	40	84.8 ± 5.5	94.4 ± 0.02
SUMSS	26.75	232	198	34	82.3 ± 5.4	58.9 ± 3.06

Note. Three wavelengths—X-ray (RASS), mm (SPT and SPT+SUMSS), radio (SUMSS)—are used to study the performance of the 4FGL association within the 2500 deg^2 sky covered by the SPT-SZ survey. The second column refers to the surface number density of each survey. The third to fifth columns represent the total number of potential counterparts for all 4FGL sources, previously identified 4FGL sources, and previously unassociated 4FGL sources, respectively. The last two columns are completeness and purity for the multiwavelength association, where the error of completeness is Poissonian and error of purity is evaluated from bootstrapping.

where N and r refer to number of samples and angular separation, respectively.

The X-ray (RASS) associations have a high purity (Figure 5, right panel), but only 54% 4FGL sources have RASS sources inside their 4σ uncertainty regions, and the RASS association is thus largely incomplete.

Matching the 4FGL sources to the SUMSS catalog, we find that 95% of the 4FGL sources have at least one SUMSS source falling inside their 4σ uncertainty region. However, as Figure 4 demonstrates, many SUMSS sources that are within the 4σ 4FGL uncertainty regions also have a high probability of being spurious associations, i.e., they lie near p = 1 and $r_{4FGL} < 4$ in p–r space. Figure 5 also demonstrates that ~1/3 of SUMSS associations have high probability of false association (p-value > 0.1) and there are often multiple possible radio counterparts within the 4σ uncertainty region. We find that ~55% of 4FGL sources have more than one potential SUMSS counterpart within the 4FGL positional uncertainty. This demonstrates that while the radio catalog has a high completeness, it also has a low purity (i.e., low confidence of a true association). When we cut the sources within $4\sigma_{4FGL}$, we are left with 232 associations and a completeness of 82%.

Matching the 4FGL sources to the SPT-SZ catalog, we find that 204 (72%) of the 4FGL sources have at least one SPT source falling inside their 4σ uncertainty regions and p-value < 0.1. Each SPT source was also cross-matched with SUMSS, within 1′ of the SPT position at 150 GHz and with p-value less than 0.1. Nearly all (99%) of the SPT sources that are located inside 4σ uncertainty regions of 4FGL have SUMSS counterparts. Only five 4FGL sources (#80, #127, #177, #211, and #225 in Appendix A; for details see thumbnails in Appendix C) have SPT counterparts but no SUMSS counterparts. When we include the faint SPT fluxes at >1σ derived from the SUMSS positions (SPT+SUMSS), we find that an additional 35 have mm counterparts within the 4σ 4FGL beams and p-value < 0.1, bringing the completeness to 85%. The mm associations also have high completeness, but because of the far lower surface density of SPT sources, the associations retain a high purity (see Figure 5, right panel). Among the 71 previously unassociated 4FGL sources in this region, 40 (56%) have mm counterparts in the SPT-SZ data.

In Table 1, we show the completeness and purity of each of the catalogs we associate with the 4FGL sources after the p-value cut. We estimate the purity for each association as discussed earlier. The completeness is defined as the fraction of 4FGL sources with a probable counterpart. In the results of multiwavelength associations, the mm (including the faint sources from the forced photometry using SUMSS priors) and radio bands have high completeness of association (85% and 82%, respectively), while the X-ray band is less than half complete (48%).

We thus conclude that the SPT+SUMSS is the most efficient means to identify 4FGL sources, as it maximizes both completeness and purity. Almost all of the SPT-identified sources (99%) have corresponding SUMSS counterparts that appear to be flat spectrum at mm and radio wavelengths (Figure 7).

The results of multiwavelength associations demonstrate the promise of mm association to identify γ-ray sources. Thus, the combination of SUMSS (radio) and SPT (mm) associations (SPT+SUMSS) can best characterize the 4FGL sources because of the high certainty and high completeness of γ-ray association with joint mm and radio counterparts. For the previously identified 4FGL sources without SPT+SUMSS counterparts, we find that three of them are pulsars, one is a faint BL Lac, and the rest are undetermined blazar candidates with X-ray emission.

3.3. The Construction of Our Combined 4FGL Multiwavelength Catalog

To summarize the previous sections, we adopt the following criteria to select multiwavelength counterparts of 4FGL sources for the analyses in this work (see Figure 2): we select SUMSS/SPT(+SUMSS)/RASS counterparts within $4\sigma_{4FGL}$ and p-value < 0.1 as the 4FGL associated counterparts.

The 4FGL-SUMSS cross-matching, while the most complete, is often degenerate with multiple possible associations. Recall that to help break the degeneracy of multiple possible SUMSS counterparts where there is no SPT source at 4.5σ, we perform forced photometry at the SUMSS position in the SPT 150 GHz map. In this way, we are able to dig deeper into the SPT map and associate the most probable radio counterpart based on the mm flux. When there are multiple sources that meet the criteria of 4σ beams and p-value < 0.1, we adopt the source with the lowest p-value in the mm. Some examples are shown in Figure 3 to illustrate how the 4FGL sources are associated with SPT and SUMSS. Of the 239 4FGL-SPT matches, 204 sources are detected at 4.5σ in Everett et al. (2020), while the remaining 35 have had mm fluxes assigned using forced photometry using the SUMSS position as a prior. For clarity, these sources are highlighted in Figures 7 and 8, labeled as FSPT for "faint."

Now, with this catalog of multiwavelength associations in hand, we can associate the 4FGL sources with the WISE catalog to characterize their infrared emission. Naively cross-matching 4FGL with WISE is difficult because the high source

density ($\sim 10^4$ deg^{-2}) results in high contamination from spurious associations. Each 4FGL source on average has ~200 potential WISE counterparts within the 95% (2σ) uncertainty ellipse. However, SPT-selected blazars with an SUMSS counterpart can provide positional accuracy better than 15″ (Vieira et al. 2010) when the S/N is greater than 5 (Ivison et al. 2007). Using the 4FGL-SPT-SUMSS associations, we performed the 4FGL association with WISE based on the refined position and selected the most likely candidates according to their lowest p-value. When cross-matching with WISE, the p-value is especially useful to eliminate spurious false associations. We adopt WISE associations using p-value < 0.03 and separation within 9″ of the combined SPT+SUMSS position. The characterization of the infrared emission of the 4FGL sources is discussed in Section 4.3.

Nearly all the SPT counterparts (99%) of 4FGL sources also have an SUMSS counterpart, allowing us to characterize each 4FGL source with both mm and radio fluxes. In Figure 7, mm sources with radio counterparts (gray dots) are roughly separated into two classes—steep-spectrum AGNs (yellow oval) and flat-spectrum AGNs (blue oval). The majority of γ-ray sources (blue and green dots) have comparable mm and radio emission, which indicates that they are either BL Lacs or FSRQs.

4. Results and Discussion

Robust multiwavelength counterpart identification of the sources in the 4FGL γ-ray catalog is crucial for understanding the γ-ray source population and the diffuse γ-ray background. In this section we study and discuss the multiwavelength properties of Fermi γ-ray blazars, including the multiwavelength flux correlation, multiwavelength color analysis, redshift dependency, and implications for future surveys.

We adopt two approaches to study the multiwavelength properties of the 4FGL sources. The first approach directly adopts the multiwavelength associations derived from SPT+SUMSS and described in Section 3. For the second approach, we divide the 4FGL sources into two groups—previously associated 4FGL sources (ID-4FGL) and previously unassociated 4FGL sources with new mm identifications (UID-4FGL-SPT). For ID-4FGL sources (which have well-measured ~arcsecond associated astrometry), we apply a simple angular-separation-based cross-matching with the external multiwavelength catalogs. For UID-4FGL sources, i.e., the ones without a previous counterpart association, we use the counterpart associations found in this work using SPT+SUMSS. Both methods—using either the provided cross-matching from the 4FGL catalog or our own independent cross-matching using SPT+SUMSS—produce qualitatively similar results. For the rest of the figures in this paper, for the ID-4FGL sources we use the supplied position for multiwavelength associations, and for the UID-4FGL sources we use the UID-4FGL-SPT position derived in this work.

The spectroscopic redshift data were acquired from the NED based on the refined source positions from the multiwavelength associations. We found 75 sources (out of 239) with redshift measurements.

4.1. The γ-Ray Flux Correlation

With the cross-matched multiwavelength catalog in hand, we can study the flux correlation across bands for the 4FGL catalog. For each band, we calculate the Spearman's rank correlation coefficient (r_{SC}) of the flux correlation, and the results are shown in Figure 6. The UID-4FGL-SPT sources (black dots) are typically faint sources at all wavelengths studied here. The inclusion of these faint sources increases the completeness of the 4FGL associations.

Starting in the radio, we see that there is a slight correlation between the radio and γ-ray flux with $r_{SC} \sim 0.3$.

The mm flux is well correlated ($r_{SC} \sim 0.5$) to the γ-ray flux and can be parameterized by the following relation:

$$\frac{S_{0.1\text{-}100\mathrm{GeV}}}{10^{-13}\ \mathrm{erg\ cm^{-2}\ s^{-1}}} = 0.8 \left(\frac{S_{150\mathrm{GHz}}}{1\ \mathrm{mJy}}\right)^{1.1}. \quad (4)$$

Most of these sources are flat-spectrum AGNs, but a few sources have stronger radio emission (see 4FGL sources with $S_{150\mathrm{GHz}} > 100$ mJy outside the blue oval in Figure 7). This may be partially related to source variability and may contribute to the radio flux correlating less well than the mm flux.

The infrared flux is statistically as correlated as the mm ($r_{SC} \sim 0.5$). However, given the high density of the infrared WISE catalog, we first needed to match the 4FGL to an SPT+SUMSS source, and then to WISE in order to refine the positional uncertainty. Thus, this correlation may be biased toward the mm-detected sources.

The X-ray flux is largely uncorrelated to the γ-ray flux ($r_{SC} \sim 0$). Naively, the lack of correlation between the γ-ray and X-ray is a surprise, given their proximity along the electromagnetic spectrum, particularly relative to the radio. This is likely due to the fact that while γ-rays in the jet are always produced via inverse Compton scattering (of synchrotron photons in BL Lac, or external photons in FSRQs), the X-rays are generated via synchrotron in BL Lacs and via IC scattering in FSRQs.

Our study demonstrates that the mm band is the most efficient band to associate γ-ray blazars with multiwavelength counterparts. As shown in Section 3, RASS's X-ray sensitivity is insufficient to detect all the 4FGL counterparts, and the X-ray flux of 4FGL sources is observed to be uncorrelated to their γ-ray fluxes (Figure 6). Thus, RASS's X-ray catalog is highly incomplete in terms of associating 4FGL sources with multiwavelength counterparts. The SUMSS radio associations have a high completeness but often have multiple counterparts and are thus confused. WISE, due to its high source density, produces a large number of spurious associations and thus needs an accurate prior on the position to enable accurate source association. The mm catalog with arcminute resolution, such as the SPT catalog, provides 4FGL associations with both high completeness and high purity (see Table 1 and Figure 5).

4.2. Previously Unidentified and Faint γ-Ray Population

As shown in Figure 6, γ-ray emission is correlated to the mm emission. Thus, the brighter 4FGL sources have a higher completeness of mm associations. The previously associated 4FGL sources (ID) typically have brighter multiwavelength fluxes (see nonblack sources in Figure 6), where 94% of them are also SPT identified. The previously unassociated 4FGL sources (UID) tend to be fainter ($S_{0.1-100\mathrm{GeV}} < 10^{-11}$ erg cm^{-2} s^{-1}) at longer wavelengths (see black sources in Figure 6), where only 56% of them are SPT identified. (See Table 1 for a summary of these associations.) In addition, as can be seen in Figure 8 (left), the remaining 4FGL sources

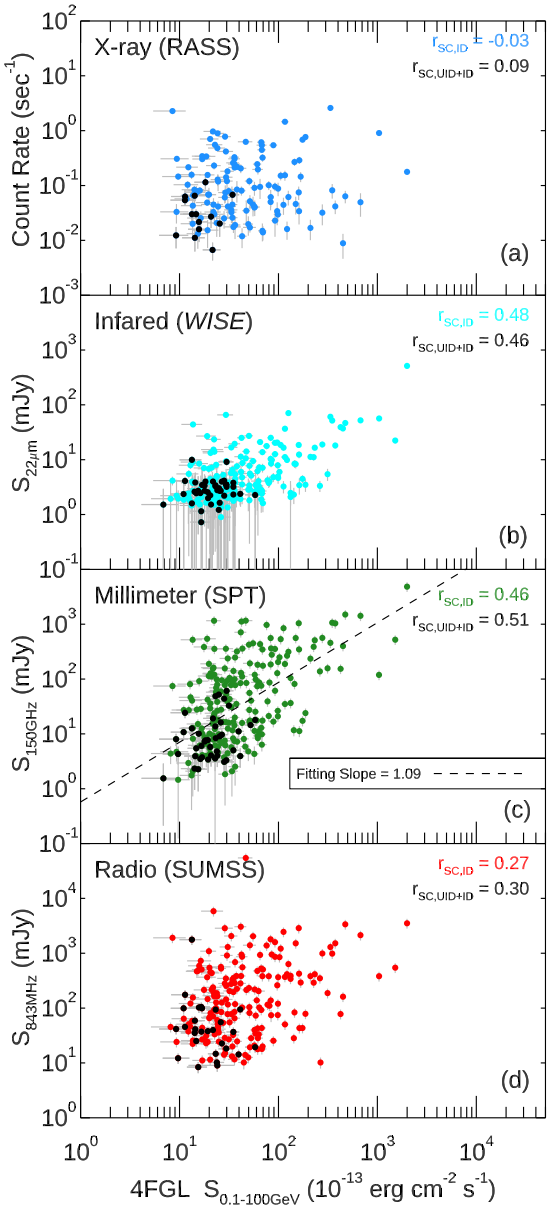

Figure 6. Flux correlations between 4FGL and other surveys (X-ray: blue; infrared: light blue; mm: green; radio: red), where black dots indicate previously unassociated 4FGL sources with mm counterparts. The Spearman's rank correlation coefficient (r_{SC}) of the flux correlation is shown in the upper right corner of each plot. Note that $r_{SC,ID}$ refers to previously associated 4FGL sources and $r_{SC,UID+ID}$ counts both previously associated and extra mm-identified 4FGL sources. (a) As most of the 4FGL-SPT blazars are flat-spectrum AGNs, the r_{SC} in the radio band should be similar to that of the mm band. However, r_{SC} in the radio band is significantly lower than the mm band because some 4FGL-SPT blazars have excess radio emission compared with most flat-spectrum sources (see Figure 7). (b) The mm and γ-ray bands are highly correlated, which is consistent with previous studies of multiwavelength associations of 4FGL sources. The dashed line represents least-squares fitting between the fluxes in the two bands. (c) The infrared band has comparable correlation to the γ-ray band as the mm band. However, the association between 4FGL and WISE has been refined by first matching to SPT because normal cross-matching would be heavily contaminated by the spurious associations due to the high source number density of WISE (~10 deg^{-2}). (d) Unlike any other wavelengths, the X-ray fluxes are uncorrelated with γ-ray fluxes. This may be because the γ-ray traces the jet while the X-ray traces the coronal region of the AGN (Ghisellini et al. 2017).

without SPT identification are mostly faint γ-ray sources ($S_{0.1-100GeV} \lesssim 5 \times 10^{-12}$ erg cm^{-2} s^{-1}), which might explain why they have remained unassociated thus far. Therefore, the identification of the remaining unassociated 4FGL blazars will be further completed by either deeper catalogs from upcoming surveys in mm wavelengths (e.g., SPT-3G, Simons Observatory, CMB-S4) or dedicated pointed observations with, e.g., ALMA, SMA, or NOEMA.

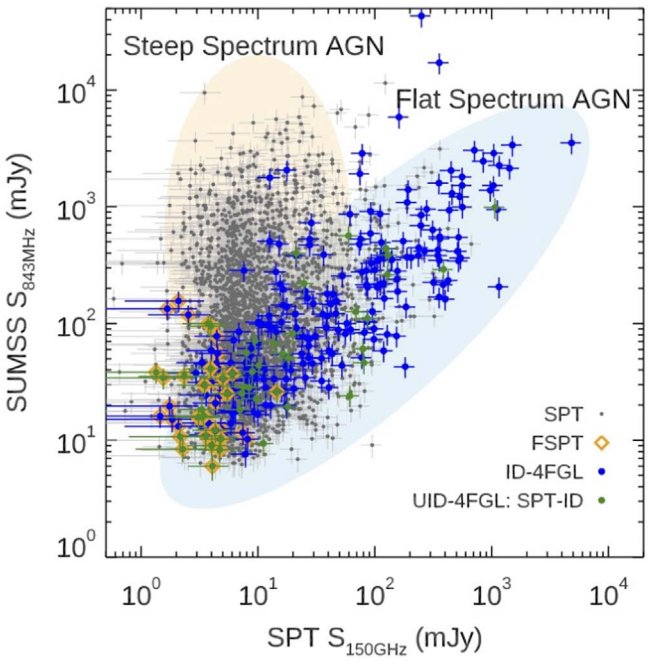

Figure 7. The flux–flux plot showing the radio flux density at 843 MHz from the SUMSS survey vs the SPT flux density at 2 mm (150 GHz) for all SPT-selected sources. The gray dots represent all the mm sources with radio counterparts. The blue/green dots represent those with previous known/unknown γ-ray detection. The orange diamonds represent faint mm sources with fluxes assigned by forced photometry using positional priors from the SUMSS radio catalog. Note that the steep-spectrum AGNs roughly lie within the yellow oval and run up the vertical axis clustered around S_{150GHz} = 10 mJy, while the flat-spectrum AGNs lie within the blue oval, which is nearly diagonal with slope = 1.239. 4FGL sources are selected if they have both SPT and SUMSS counterparts. These sources are shown in green and blue. Note that the total number of both blue and green dots in the plot is 265. This is because some 4FGL sources have multiple mm–radio counterparts as illustrated in Figure 3. Similar to Figure 1, the blue points are previously associated 4FGL sources, while the green points are previously unassociated 4FGL sources that have SPT counterparts. The majority of 4FGL sources are flat-spectrum AGNs.

In Figure 7 we plot the radio versus mm flux for all sources in the SPT catalog with a radio counterpart and highlight the sources with γ-ray counterparts. Some flat-spectrum AGNs with strong mm emission (S_{150GHz} > 100 mJy) are still undetected in γ-ray. Roughly half of them are γ-ray-quiet blazars and can also be found in CGRaBS (see Healey et al. 2008; Paliya et al. 2017) or ROMA-BZCAT (Massaro et al. 2015). The rest of them are also blazar-like but lack γ-ray detection. The γ-ray-quiet blazars are often associated with small Doppler factors and high disk dominance (Paliya et al. 2017). As noted by several authors (Dermer 1995; Paliya et al. 2017; Ghisellini et al. 2017), there are two important selection effects that could make a luminous but high-redshift blazar not detected by Fermi: (1) Luminous sources usually have the high-energy peaks of their SEDs shifted to lower energies, even as measured in the source frame, which is in addition to the effect of redshift itself. (2) These sources may be highly beamed at γ-rays and slightly misaligned, making them currently undetected by Fermi-LAT. Unfortunately, we do not have the data necessary to resolve this issue at this time, but, for instance, a stacking analysis could be done in the future.

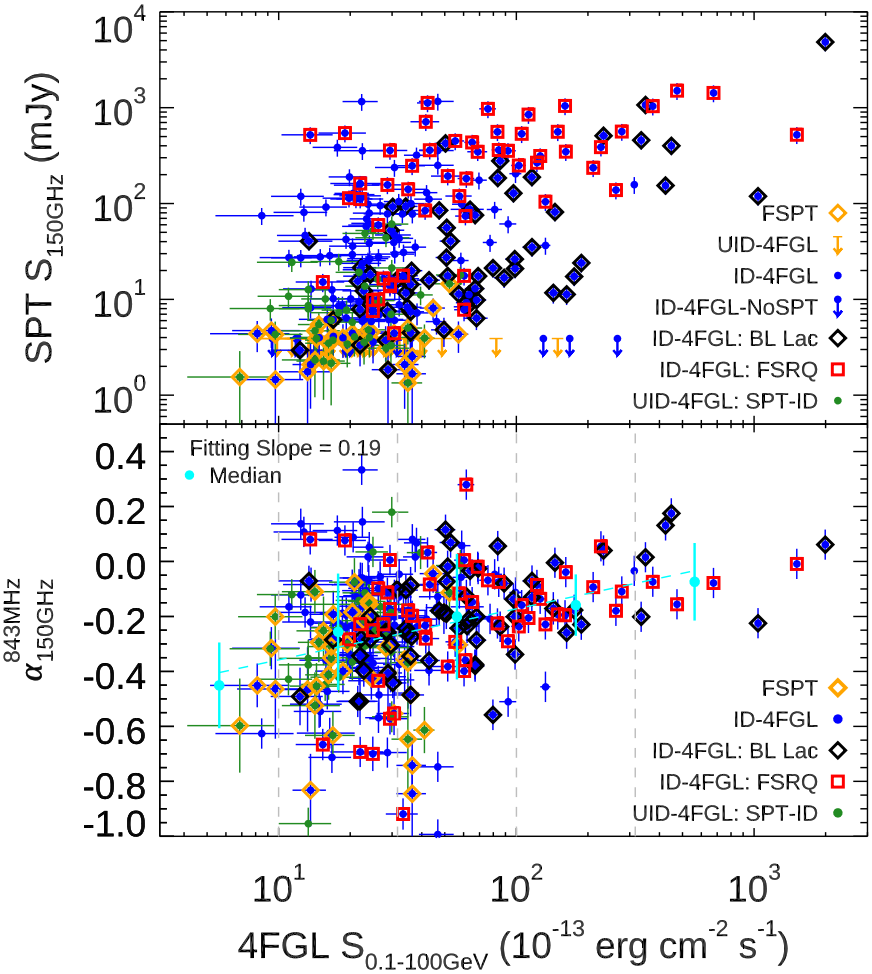

Figure 8. Top panel: mm and γ-ray flux correlation with each source labeled. Source types are labeled by their identities (previously identified 4FGL source: blue d BL Lac: black diamond; FSRQ: red square; unassociated 4FGL source: green dot; faint mm sources: orange diamonds). The previously identified 4FGL sources without mm detections (ID-4FGL-NoSPT) and the remaining unidentified 4FGL sources (UID-4FGL) are indicated by blue and orange arrows, respectively, upper limits from SPT-SZ. Note that three bright ID-4FGL-NoSPT sources ($S_{0.1\text{-}100GeV} > 10^{-11}$ erg cm^{-2} s^{-1}) in blue arrows are previously identified pulsars and therefore fail to be identified by SPT. Within associated 4FGL sources, FSRQs are more likely to be brighter than BL Lacs in mm wavelength. Most unassociated 4FGL sources are faint in both mm and γ-ray bands, which indicates that source identification might be limited by the sensitivity of the current generation of surveys. Bottom panel: the mm–radio spectral index ($\alpha^{848\ MHz}_{150\ GHz}$) as a function of γ-ray flux. Sources are labeled the same way as in the left panel. Cyan dots denote the median and standard deviations of the spectral index in each logarithmic bin of γ-ray flux. As shown in the plot, sources with brighter γ-ray fluxes are more likely to have flatter spectra except a few sources with γ-ray flux around 10^{-11} erg cm^{-2} s^{-1}. These outliers have excess radio emission compared with normal flat-spectrum AGNs. Among these sources, some might have extra radio emission from nearby radio lobes, some are just ambiguous cross-matching that blends several radio counterp and some have valid multiband counterparts and need further investigation.

4.3. Gamma-Ray Blazars in Radio, Millimeter, and Mid-IR

By using multiwavelength profiles and labeling the source type of associated 4FGL sources, we studied how the spectral characteristics influence the patterns in multiple parameter spaces.

First, we looked into the SPT-identified 4FGL sources within the SPT-SZ field in the radio, mm, and γ-ray band fluxes. FSRQs and BL Lacs have already been classified in the 4FGL catalog based on their optical spectra (Abdollahi et al. 2020). As shown in the left panel of Figure 8, FSRQs are generally brighter than BL Lacs in mm wavelengths but indistinguishable in γ-ray. The right panel demonstrates how the spectral indices vary with γ-ray flux, where the spectral index is defined as

$$a^{843MHz}_{150GHz} = \frac{\log \frac{S_{150GHz}}{S_{843MHz}}}{\log \frac{150GHz}{843MHz}}. \quad (5)$$

A flat-spectrum from mm to radio corresponds to $a^{843MHz}_{150GHz} = 0$. As shown in the right panel of Figure 8, the radio spectral index of bright γ-ray sources tends to be more flat, presumably because the viewing angle is more aligned with the center of the jet, and thus the observed emission is dominated by the central engine of the jet. As γ-ray flux decreases below ~5 × 10^{-12} erg cm^{-2} s^{-1}, flat-spectrum and steep-spectrum AGNs are heavily mixed together (S_{843MHz} and S_{150GHz} ≲ 100 mJy in Figure 7), so the spectral index exhibits a higher scatter at lower γ-ray fluxes. Most of the sources (<10^{-11} erg cm^{-2} s^{-1}) have a steeper (i.e., less flat) radio spectral index because they are less jet-dominated. The radio emission from jets likely originates from an optically thick regime. Therefore, there could be additional radio emission if the surface is large. However, the jet is optically thin in the mm, where mm emission and γ-ray emission are likely to be produced cospatially in the compact emission region in the jets (Meyer et al. 2019). This is consistent with the higher flux correlation between mm and γ-ray than with the radio (see Figure 6).

Next, we studied the 4FGL sources with joint mm and infrared counterparts in WISE color space. The WISE

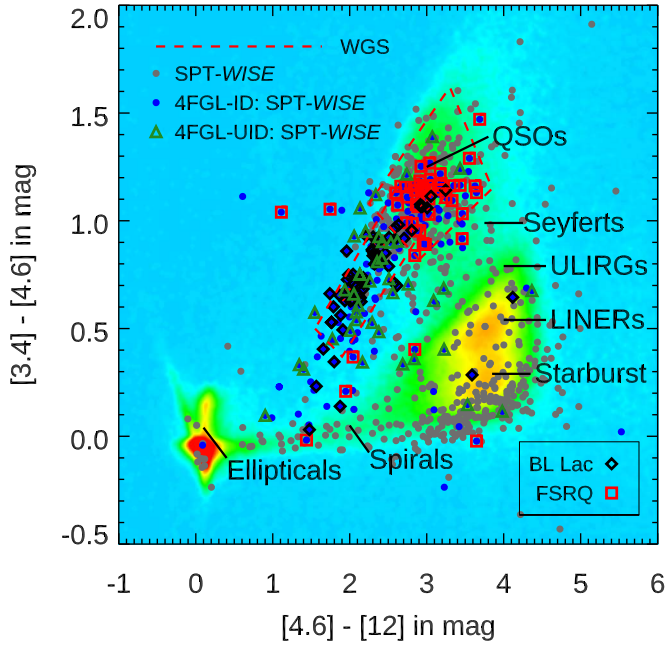

Figure 9. WISE color analysis. The background color map is based on the number source density in WISE color space. This color map contours the classes of WISE objects (see also Wright et al. 2010). On the background color map, each dot marks the SPT-selected source. These sources are also labeled by their identifications (previously associated 4FGL source: blue dot; previously unassociated 4FGL source with mm counterpart: green triangle; BL Lac: black diamond; FSRQ: red square). Red dashed lines outline the WGS (Massaro et al. 2012). Most of the mm associations lie inside the WGS, which indicates the consistency of mm correlation and WGS parameterization. Besides, the mm cross-matching provides more intrinsic associations and pinpoints the valid outliers outside WGS in WISE color space.

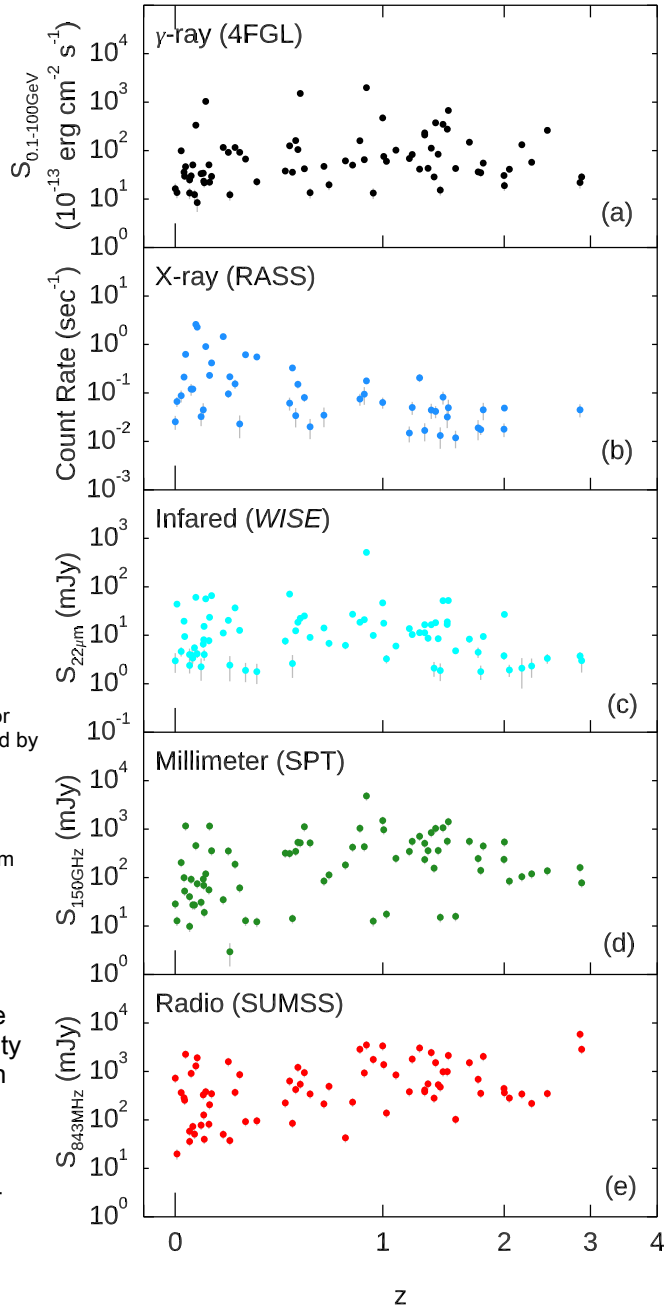

Figure 10. Multiwavelength flux density as a function of redshift. Most wavelengths (radio, mm, infrared, and γ-ray) show no apparent correlations between flux density and redshift, while in X-rays the upper bound of count rate declines for the fainter sources. Therefore, at most wavelengths, flat-spectrum AGNs are equally likely to be detected given the flux above the threshold of flux detection. In the X-rays, the extra flux dependence constraining the upper bound is due to the relative shallow depth of RASS. Either the bright X-ray sources at high redshift are less likely to be detected by RASS, or the origin of X-ray emission can be different from other wavelengths.

two-color diagram has clear patterns for the classes of WISE objects (see also Wright et al. 2010). As shown in Figure 9, the background color contours represent the source number density of WISE objects, with density increasing from blue to red. Each population of WISE objects is labeled on the diagram. For the SPT sources with WISE counterparts, some of them have infrared colors indicative of being AGN dominated, while others have a substantial component of starlight from an early-type host galaxy. Many other SPT sources that are not γ-ray emitters have very blue [3.4]–[4.6] colors, which is indicative of redshifts reaching up to around 1. The red dashed lines outline the region of the WISE Gamma-ray Strip (WGS; Massaro et al. 2012), which indicates the location of the known blazars from ROMA-BZCAT in WISE color space. The majority of SPT-identified blazars with γ-ray emission are located within both the QSO population and WGS. We find general consistency between our association results with WISE source classification and WGS parameterization. Moreover, since the mm is efficient at associating γ-ray-loud flat-spectrum AGNs, it also provides a method to validate outliers from the WGS region and also pinpoint other possible populations that contain γ-ray emission along with infrared emission.

4.4. The Redshift Distribution of Gamma-Ray Blazars

With previous multiwavelength associations, we obtained the redshifts for 31% (75 out of 239 sources) of associated 4FGL sources by cross-matching the NED database. An important caveat to the discussion below is that this sample is highly spectroscopically incomplete and could be highly susceptible to selection biases. For instance, the sources with spectroscopic redshifts are presumably biased toward being optically bright and having strong emission lines. A future spectroscopic survey, or a dedicated targeted spectroscopic campaign, would be needed before any strong conclusions are drawn from this particular discussion.

In Figure 10 we investigate the redshift dependence on the multiwavelength detection of 4FGL sources. With the exception of the X-ray band, the majority of multiwavelength fluxes

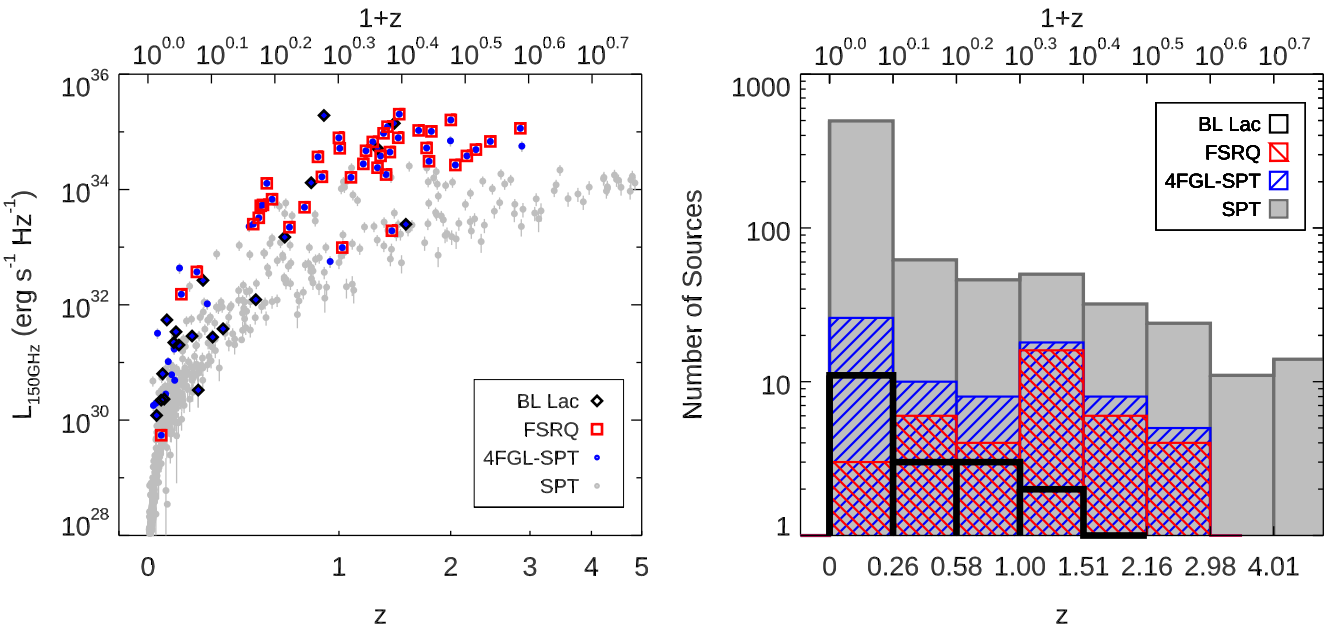

Figure 11. Left panel: specific luminosity in 150 GHz as a function of redshift. We have assumed a ΛCDM cosmology with $\Omega_M = 0.27$, $\Omega_\Lambda = 0.73$, and $H_0 = 71$ km s^{-1} Mpc^{-1}. Gray dots represent all the SPT sources with redshift measurements. Those with 4FGL counterparts (4FGL-SPT) are covered by blue dots. We also label the blazar type for each 4FGL-SPT source if it is classified in the catalog. Given the same redshift, mm-identified 4FGL sources (flat-spectrum AGNs) are brightest, where the specific luminosity is above the threshold of mm detection by orders of magnitude. This is resulting from the mixing of two types of sources (flat-spectrum and steep-spectrum AGNs) and the selection bias of redshift. Details are discussed in Section 4. We can roughly distinguish the population of FSRQs and BL Lacs by their mm specific luminosity. Right panel: histogram of redshift distribution. The label colors are consistent with the left panel, and redshifts are binned logarithmically. This histogram shows that the populations of FSRQs and BL Lacs can be distinguished by their redshift measurements as well. FSRQs mostly observed with higher redshift than BL Lacs. This distinction should come from the detection bias of optical spectrum measurement. In general, FSRQs have strong emission lines in optical broadband, while the broadband spectra of BL Lacs have weak emission lines or are even featureless.

of 4FGL sources have no clear redshift dependence. In the left panel of Figure 11, SPT-identified 4FGL sources (blue) are demonstrably more luminous in the mm band than the sources not detected in 4FGL. In addition to the 4FGL-SPT sources, we also label the 4FGL classification of FSRQ (red) and BL Lac (black) and histogram the redshift distribution based on their types. In the right panel of Figure 11, BL Lacs are mostly observed with lower redshift than FSRQs. This distinction may be due to an observational bias, as BL Lacs generally have weak optical emission lines.

5. Conclusion

1. We have shown that the mm flux detected by SPT from flat-spectrum AGNs is the most effective method currently available for identifying extragalactic 4FGL γ-ray sources and predicting the possible γ-ray emission. The SPT detection, combined with an accurate source position, finds 4FGL sources with the highest completeness rate and, at the same time, the lowest contamination rate.
2. The effectiveness of the SPT+SUMSS selection has been demonstrated first by confirming the association of 94% (199 out of 211 sources) of already-known 4FGL sources across the 2500 deg^2 SPT-SZ survey field. It is then applied to identify 40 new sources for which 4FGL did not previously have a counterpart at lower energies (out of 71 previously unidentified sources within the SPT-SZ survey field). Deeper and wider mm surveys will soon be available, which will greatly complete these 4FGL associations.
3. We have used multiwavelength data to explain why SPT is more effective at finding associations for γ-ray sources. Our interpretation is that the mm flux is closely correlated with the γ-ray flux (Meyer et al. 2019) because both have a common origin in the jet.
4. SPT has shown its extraordinary ability to track jet-dominant AGNs and find blazar-like objects. Therefore, SPT can also complete the sampling of γ-ray-quiet blazars. SPT has detected 60 bright mm emitters ($S_{150GHz} > 100$ mJy) that do not currently have any γ-ray detection. Roughly half of them are γ-ray-quiet blazars and can be found in CGRaBS (Paliya et al. 2017) or ROMA-BZCAT (Massaro et al. 2015). The rest of them are also blazar-like sources and lack multiwavelength detection.
5. SPT-3G (Benson et al. 2014) will survey 1500 deg^2 of southern sky 10× deeper and with polarization sensitivity. The DOE has recently begun planning a next-generation experiment (CMB-Stage 4; Abazajian et al. 2016) to cover the entire extragalactic sky. Thus, this initial study enables us to prepare forecasts for the next generation of SPT surveys and CMB experiments that will extend this technique to greater sensitivities and across the entire sky. With much more powerful data sets from SPT-3G and CMB-S4, we should be able to complete the association of the remaining unassociated 4FGL sources and also study the light curves of 4FGL blazars in both mm and γ-ray. The variability analysis will directly answer whether mm emission and γ-ray emission from 4FGL blazars are intrinsically correlated, which is indicative of the radiation process inside relativistic jets.

While deeper future surveys in the X-ray (e.g., eROSITA), the radio (e.g., VLASS, MeerKAT, ASKAP, SKA), and the

mm regime (SPT-3G, CMB-S4) will help advance this work and improve statistics, we believe that these general characteristics of the multiwavelength associations with γ-ray catalogs will remain largely unchanged.

The authors would like to thank Tom Crawford and Gil Holder for helpful conversations and crucial insights that greatly improved this paper. This work was partially supported by NASA Fermi Guest Observer Program No. 101261. The SPT is supported by the NSF through grant OPP-1852617. J.D.V. acknowledges support from the NSF under grants AST-1715213 and AST-1716127. J.D.V. acknowledges support from an A. P. Sloan Foundation Fellowship. M.A.A. and J.D.V. acknowledge support from the Center for AstroPhysical Surveys at the National Center for Supercomputing Applications in Urbana, IL. This research has made use of NASA's Astrophysics Data System Bibliographic Services. This research has made use of the NASA/IPAC Extragalactic Database (NED), which is operated by the Jet Propulsion Laboratory, California Institute of Technology, under contract with the National Aeronautics and Space Administration.

Appendix A
4FGL-SPT Association Table

We list all 282 4FGL sources within the 2500 deg^2 SPT-SZ survey field in Table 2. For each 4FGL source, all the SPT counterparts are listed on the right. The index is based on the sequence of the energy flux (100 MeV–100 GeV) from high to low. In this table, 4FGL sources with "*" represent that the source has no associated counterpart in the original 4FGL catalog. Most of SPT sources have detections greater than 4.5σ except those SPT sources whose name starts with "F" (for "faint"), which represent the detection less than 4.5σ but greater than 1σ. Recall that the uncertainty of mm flux includes mm variability, statistical and systematic noises, while the uncertainty of 4FGL energy flux is just the statistical noise. Source separations are listed in units of arcmin (d_1) and σ of the 4FGL positional uncertainty (d_2).

Table 2
282 4FGL Sources within 2500 deg^2 SPT–SZ Survey Field

Index	4FGL Name	$S_{0.1-100GeV}$ (10^{-13} erg cm^{-2} s^{-1})	SPT Name	S_{150GHz} (mJy)	dr_1 (arcmin)
0	4FGL J0538.8-4405	1993.0 ± 26.0	SPT-S J053850-4405.1	4843.0 ± 970.2	0.09
1	4FGL J2329.3-4955	1513.6 ± 18.2	SPT-S J232920-4955.6	522.1 ± 104.6	0.41
2	4FGL J0449.4-4350	1039.1 ± 25.9	SPT-S J044924-4350.0	119.3 ± 23.9	0.29
3	4FGL J2056.2-4714	675.1 ± 12.5	SPT-S J205616-4714.8	1424.9 ± 285.4	0.63
4	4FGL J0210.7-5101	474.0 ± 10.2	SPT-S J021045-5101.0	1504.4 ± 301.4	0.32
5	4FGL J0532.0-4827	448.8 ± 15.1	SPT-S J053158-4827.6	400.3 ± 80.2	0.29
6	4FGL J2139.4-4235	424.3 ± 14.5	SPT-S J213924-4235.4	154.0 ± 30.9	0.11
7	4FGL J0245.9-4650	374.9 ± 9.2	SPT-S J024600-4651.2	1036.5 ± 207.6	0.47
8	4FGL J0334.2-4008	349.3 ± 10.7	SPT-S J033413-4008.4	1068.5 ± 214.1	0.27
9	4FGL J2009.4-4849	335.0 ± 13.1	SPT-S J200925-4849.7	457.8 ± 91.7	0.31
10	4FGL J2141.7-6410	313.4 ± 10.0	SPT-S J214145-6411.1	157.3 ± 31.5	0.50
11	4FGL J0309.9-6058	277.7 ± 8.7	SPT-S J030956-6058.6	563.7 ± 112.9	0.32
12	4FGL J2241.7-5236	266.1 ± 12.8	L	L	L
13	4FGL J0228.3-5547	262.4 ± 16.2	SPT-S J022821-5546.0	138.2 ± 27.7	1.53
14	4FGL J0516.7-6207	232.7 ± 10.4	SPT-S J051644-6207.0	510.1 ± 102.2	0.49
15	4FGL J2328.3-4036	226.9 ± 11.0	SPT-S J232818-4035.1	387.7 ± 77.7	1.06
16	4FGL J0526.2-4830	210.4 ± 11.3	SPT-S J052616-4830.6	236.1 ± 47.3	0.23
17	4FGL J0209.3-5228	187.6 ± 9.7	SPT-S J020921-5229.3	24.0 ± 4.9	0.66
18	4FGL J0543.9-5531	175.1 ± 11.0	SPT-S J054357-5532.1	17.3 ± 3.6	0.34
19	4FGL J0437.2-4715	167.7 ± 6.0	L	L	L
20	4FGL J0051.2-6242	162.7 ± 10.8	SPT-S J005115-6241.9	11.3 ± 2.5	0.34
21	4FGL J0030.3-4224	161.4 ± 6.4	SPT-S J003017-4224.8	347.6 ± 69.6	0.98
22	4FGL J0455.7-4617	160.2 ± 7.3	SPT-S J045550-4615.9	1043.0 ± 209.0	1.45
23	4FGL J2126.3-4605	149.3 ± 6.6	SPT-S J212630-4605.6	560.1 ± 112.2	1.40
24	4FGL J2039.5-5617*	149.3 ± 8.3	L	L	L
25	4FGL J2103.8-6233	145.3 ± 8.5	SPT-S J210337-6232.4	81.6 ± 16.4	1.61
26	4FGL J0143.7-5846	143.1 ± 8.6	SPT-S J014347-5845.7	11.7 ± 2.7	0.59
27	4FGL J2052.2-5533	132.6 ± 6.5	SPT-S J205213-5533.1	36.6 ± 7.4	0.68
28	4FGL J2135.3-5006	132.5 ± 6.2	SPT-S J213521-5006.7	104.6 ± 21.0	0.71
29	4FGL J0101.1-6422	129.9 ± 5.4	L	L	L
30	4FGL J0236.8-6136	125.9 ± 6.7	SPT-S J023652-6136.1	313.8 ± 62.9	0.70
31	4FGL J0433.6-6030	122.0 ± 6.5	SPT-S J043333-6030.0	266.9 ± 53.5	0.73
32	4FGL J2324.7-4041	116.4 ± 10.2	SPT-S J232444-4040.8	35.0 ± 7.2	0.22
33	4FGL J2325.4-4800	116.2 ± 6.8	SPT-S J232527-4800.2	188.8 ± 37.8	0.57
34	4FGL J0303.6-6211	112.5 ± 6.0	SPT-S J030350-6211.4	847.4 ± 169.8	1.04
			SPT-S J030337-6214.6	22.5 ± 4.6	3.32
35	4FGL J2235.3-4836	105.3 ± 5.4	SPT-S J223513-4835.9	534.3 ± 107.0	1.45
36	4FGL J0507.7-6104	102.4 ± 7.3	SPT-S J050754-6104.6	249.5 ± 50.0	1.29
37	4FGL J0133.1-5201	99.2 ± 5.7	SPT-S J013305-5200.1	204.5 ± 41.0	1.39
38	4FGL J0343.2-6444	98.7 ± 6.0	SPT-S J034320-6442.8	20.9 ± 4.3	1.36
39	4FGL J0602.8-4019	98.5 ± 8.7	SPT-S J060250-4018.7	26.3 ± 5.4	1.02
40	4FGL J0424.9-5331	97.2 ± 5.2	SPT-S J042504-5331.8	128.1 ± 25.7	0.70
41	4FGL J2007.9-4432	92.3 ± 7.6	SPT-S J200755-4434.6	61.3 ± 12.3	2.51
42	4FGL J0515.6-4556	92.2 ± 7.3	SPT-S J051544-4556.6	354.6 ± 71.0	1.17
43	4FGL J2221.5-5225	88.8 ± 8.2	SPT-S J222129-5225.5	16.8 ± 3.6	0.68
44	4FGL J0438.9-4521	85.5 ± 6.5	SPT-S J043900-4522.3	278.3 ± 55.8	0.87
45	4FGL J2336.6-4115	84.3 ± 5.6	SPT-S J233633-4115.3	362.1 ± 72.6	1.06

Table 2
(Continued)

Index	4FGL Name	$S_{0.1-100GeV}$ (10^{-13} erg cm^{-2} s^{-1})	SPT Name	S_{150GHz} (mJy)	dr_1 (arcmin)
46	4FGL J2022.3-4513	83.5 ± 6.1	SPT-S J202226-4513.4	184.9 ± 37.1	0.90
47	4FGL J2207.5-5346	83.2 ± 5.1	SPT-S J220743-5346.5	559.6 ± 112.1	1.40
48	4FGL J2347.9-5106*	82.3 ± 5.3	L	L	L
49	4FGL J0647.7-6058	81.0 ± 6.0	SPT-S J064740-6058.0	86.6 ± 17.4	0.74
50	4FGL J0331.3-6156	79.7 ± 5.8	SPT-S J033118-6155.3	21.2 ± 4.4	0.97
51	4FGL J2321.7-6438	77.5 ± 5.2	SPT-S J232142-6438.1	39.2 ± 8.0	0.56
52	4FGL J2357.8-5311	75.9 ± 6.1	SPT-S J235753-5311.2	971.8 ± 194.7	0.41
53	4FGL J0608.9-5456	69.6 ± 5.5	SPT-S J060848-5456.6	175.2 ± 35.1	1.21
54	4FGL J0021.9-5140	69.0 ± 5.3	SPT-S J002159-5140.4	17.5 ± 3.7	0.06
55	4FGL J0540.8-5415	68.8 ± 6.6	SPT-S J054045-5418.3	346.6 ± 69.4	3.00
56	4FGL J0156.9-5301	68.0 ± 6.7	SPT-S J015657-5302.0	9.8 ± 2.3	0.35
57	4FGL J0506.9-5435	67.9 ± 7.8	SPT-S J050658-5435.0	6.4 ± 1.6	0.20
58	4FGL J0244.6-5819	67.0 ± 6.4	SPT-S J024439-5819.8	12.9 ± 2.8	0.41
59	4FGL J0628.8-6250	67.0 ± 5.3	SPT-S J062857-6248.8	75.8 ± 15.2	1.70
60	4FGL J0004.4-4737	65.1 ± 4.7	SPT-S J000435-4736.3	433.9 ± 86.9	1.89
61	4FGL J0314.3-5103	63.9 ± 5.2	SPT-S J031425-5104.4	86.4 ± 17.4	1.27
62	4FGL J2251.5-4928	63.1 ± 6.8	SPT-S J225129-4929.1	11.2 ± 2.5	1.03
63	4FGL J0450.3-4419	62.9 ± 10.0	SPT-S J045001-4418.2	86.9 ± 17.5	3.19
64	4FGL J2322.8-4916	62.0 ± 7.5	SPT-S J232254-4916.6	8.4 ± 2.1	0.76
65	4FGL J0316.2-6437	61.6 ± 6.0	SPT-S J031613-6437.5	9.2 ± 2.1	0.19
66	4FGL J0231.2-4745	61.5 ± 5.0	SPT-S J023112-4746.1	182.2 ± 36.5	0.75
67	4FGL J0451.8-4651	61.1 ± 5.8	SPT-S J045153-4653.2	74.0 ± 14.9	1.96
68	4FGL J0413.1-5332	60.3 ± 5.5	SPT-S J041313-5331.9	17.6 ± 3.7	1.42
			SPT-S J041303-5333.8	7.8 ± 1.9	1.06
69	4FGL J2132.0-5418	58.9 ± 5.2	SPT-S J213208-5420.4	98.4 ± 19.7	1.75
70	4FGL J0032.3-5522	58.4 ± 4.5	SPT-S J003210-5522.5	25.4 ± 5.3	1.20
71	4FGL J2240.3-5241*	58.1 ± 12.2	SPT-S J224016-5241.3	18.0 ± 3.8	0.59
72	4FGL J0157.7-4614	57.6 ± 7.3	SPT-S J015751-4614.4	119.6 ± 24.0	1.24
73	4FGL J2317.4-4533	57.2 ± 5.1	SPT-S J231731-4533.9	11.4 ± 2.6	1.01
74	4FGL J0525.6-6013	57.0 ± 5.7	FSPT-S J052542-6013.6	4.3 ± 0.9	0.14
75	4FGL J0050.0-5736	55.3 ± 5.0	SPT-S J004959-5738.4	449.6 ± 90.1	1.58
76	4FGL J0556.2-4352	52.9 ± 5.3	SPT-S J055617-4351.9	40.5 ± 8.2	0.23
77	4FGL J0059.4-5654*	52.3 ± 6.9	FSPT-S J005926-5657.1	14.5 ± 2.9	2.61
78	4FGL J0608.1-6028	51.5 ± 7.7	SPT-S J060755-6031.8	193.3 ± 38.7	3.58
79	4FGL J0335.1-4459	51.4 ± 5.0	SPT-S J033514-4459.5	17.6 ± 3.7	1.01
80	4FGL J0514.6-4408	50.9 ± 3.5	SPT-S J051422-4403.0	16.5 ± 3.6	5.73
81	4FGL J2250.4-4206	50.9 ± 4.7	SPT-S J225022-4206.2	55.9 ± 11.3	0.73
82	4FGL J0325.5-5635	50.8 ± 5.0	SPT-S J032522-5635.6	27.3 ± 5.6	1.17
83	4FGL J2315.6-5018	50.3 ± 5.1	SPT-S J231545-5018.6	424.2 ± 85.0	0.96
84	4FGL J0310.6-5017	49.6 ± 5.8	FSPT-S J031034-5016.5	4.8 ± 1.0	0.95
85	4FGL J2133.1-6432*	48.7 ± 4.8	L	L	L
86	4FGL J0357.0-4955	47.3 ± 4.3	SPT-S J035658-4955.7	84.9 ± 17.0	0.62
87	4FGL J0519.6-4544	46.7 ± 7.8	SPT-S J051948-4546.6	1163.6 ± 233.1	2.83
			SPT-S J051927-4545.8	356.7 ± 71.5	2.10
			SPT-S J052005-4547.3	250.4 ± 50.2	5.65
88	4FGL J0433.7-5725	46.1 ± 4.6	SPT-S J043343-5726.4	5.9 ± 1.6	0.80
89	4FGL J2034.8-4200	44.6 ± 5.4	FSPT-S J203451-4200.4	8.1 ± 1.6	0.43

Table 2
(Continued)

Index	4FGL Name	$S_{0.1-100GeV}$ (10^{-13} erg cm^{-2} s^{-1})	SPT Name	S_{150GHz} (mJy)	dr_1 (arcmin)
90	4FGL J2231.0-4416	43.2 ± 4.2	SPT-S J223056-4416.4	359.9 ± 72.1	1.11
91	4FGL J2040.0-5737	42.9 ± 5.7	SPT-S J204000-5735.2	111.1 ± 22.3	1.93
92	4FGL J0537.7-5717	42.9 ± 4.7	SPT-S J053749-5718.3	15.9 ± 3.3	1.37
93	4FGL J0253.2-5441	42.3 ± 4.1	SPT-S J025329-5441.8	1121.4 ± 224.6	2.37
			SPT-S J025307-5441.1	2.2 ± 0.6	0.98
94	4FGL J0025.7-4801	41.9 ± 4.6	SPT-S J002545-4803.8	129.8 ± 26.0	2.70
95	4FGL J2329.3-4733	41.6 ± 5.7	SPT-S J232918-4730.3	712.6 ± 142.8	3.10
96	4FGL J0625.8-5441	41.3 ± 5.5	SPT-S J062552-5438.9	84.5 ± 17.0	2.64
97	4FGL J0022.0-5921*	41.1 ± 4.2	FSPT-S J002127-5919.8	3.9 ± 0.8	4.95
98	4FGL J2342.4-4739*	40.3 ± 4.6	L	L	L
99	4FGL J2056.4-5922*	39.5 ± 4.9	SPT-S J205624-5917.4	11.1 ± 2.4	4.66
100	4FGL J2333.1-5527*	39.4 ± 4.4	L	L	L
101	4FGL J0509.9-6417	38.2 ± 4.5	SPT-S J050957-6417.9	7.2 ± 1.9	0.57
102	4FGL J2358.0-4601	38.0 ± 4.4	SPT-S J235802-4555.2	319.3 ± 64.0	5.85
103	4FGL J0303.4-5232	37.5 ± 4.2	SPT-S J030328-5234.5	35.1 ± 7.1	2.51
104	4FGL J0643.2-5356	36.5 ± 4.9	SPT-S J064319-5358.7	77.6 ± 15.6	2.61
105	4FGL J2130.4-4241	36.5 ± 5.2	FSPT-S J213017-4244.4	1.7 ± 0.3	3.33
			FSPT-S J213017-4243.3	2.5 ± 0.5	2.29
106	4FGL J0051.5-4220	36.4 ± 4.8	SPT-S J005109-4226.5	247.6 ± 49.6	6.99
107	4FGL J0132.8-4413	36.2 ± 4.0	SPT-S J013306-4414.4	19.9 ± 4.2	3.11
108	4FGL J0606.5-4730	36.0 ± 4.9	SPT-S J060635-4729.7	99.7 ± 20.0	0.54
109	4FGL J0003.1-5248	36.0 ± 4.9	L	L	L
110	4FGL J0226.5-4441	35.9 ± 5.0	FSPT-S J022627-4441.1	4.5 ± 0.9	1.44
			FSPT-S J022638-4441.3	7.4 ± 1.5	0.61
111	4FGL J2258.4-5524	35.9 ± 4.0	SPT-S J225819-5525.5	14.3 ± 3.0	1.16
112	4FGL J0610.9-6054	35.1 ± 6.6	SPT-S J061030-6058.6	140.6 ± 28.2	4.69
113	4FGL J0049.4-5402	35.0 ± 4.0	SPT-S J004948-5402.7	16.4 ± 3.5	3.30
114	4FGL J2054.1-4054*	35.0 ± 5.2	FSPT-S J205409-4050.4	1.3 ± 0.3	3.83
			FSPT-S J205422-4051.3	5.0 ± 1.0	3.94
115	4FGL J0604.1-4816	34.8 ± 5.2	SPT-S J060409-4817.4	8.3 ± 2.0	0.73
116	4FGL J0557.5-4452*	34.3 ± 5.7	L	L	L
117	4FGL J0528.7-5920	34.3 ± 4.2	SPT-S J052846-5919.8	11.7 ± 2.5	0.80
118	4FGL J0146.9-5202	34.2 ± 4.1	SPT-S J014648-5202.5	93.3 ± 18.7	1.12
119	4FGL J0001.6-4156	33.9 ± 4.9	FSPT-S J000133-4155.4	2.1 ± 0.4	1.72
120	4FGL J0535.1-5422*	33.8 ± 5.7	L	L	L
121	4FGL J0138.5-4613	33.5 ± 4.1	SPT-S J013834-4614.2	30.9 ± 6.3	1.22
122	4FGL J0525.4-4600	33.4 ± 5.1	SPT-S J052532-4559.8	5.7 ± 1.6	0.82
			SPT-S J052531-4557.9	17.7 ± 3.8	2.46
123	4FGL J0034.0-4116	33.1 ± 4.7	SPT-S J003404-4116.4	77.8 ± 15.6	0.29
124	4FGL J2043.9-4802*	32.2 ± 3.4	L	L	L
125	4FGL J2159.8-4751	32.1 ± 4.7	SPT-S J215958-4751.9	43.3 ± 8.8	1.59
			SPT-S J215859-4748.9	8.8 ± 2.2	8.85
126	4FGL J2343.7-5624	32.0 ± 4.3	SPT-S J234327-5626.2	104.8 ± 21.0	3.09
127	4FGL J0617.6-4028*	31.6 ± 5.8	SPT-S J061646-4021.7	32.8 ± 6.7	12.10
128	4FGL J0200.3-4109	31.5 ± 4.7	L	L	L
129	4FGL J0116.2-6153	31.4 ± 4.2	SPT-S J011619-6153.7	16.0 ± 3.4	0.56
130	4FGL J2056.4-4904	30.8 ± 6.4	SPT-S J205614-4904.1	12.5 ± 2.8	2.52

Table 2
(Continued)

Index	4FGL Name	$S_{0.1-100GeV}$ (10^{-13} erg cm^{-2} s^{-1})	SPT Name	S_{150GHz} (mJy)	dr_1 (arcmin)
			SPT-S J205714-4901.3	29.6 ± 6.1	7.91
131	4FGL J0533.1-6119	30.7 ± 5.3	SPT-S J053435-6106.2	237.6 ± 47.6	16.84
			SPT-S J053304-6115.9	6.1 ± 1.7	3.41
			SPT-S J053047-6115.4	47.0 ± 9.5	17.25
132	4FGL J0647.7-4418	30.6 ± 4.8	FSPT-S J064744-4419.7	4.4 ± 0.9	1.50
133	4FGL J2143.0-5501	30.5 ± 5.6	SPT-S J214121-5504.4	39.3 ± 8.0	14.66
134	4FGL J2319.1-4207	30.2 ± 4.2	SPT-S J231905-4206.7	92.4 ± 18.5	0.33
135	4FGL J2237.6-5126*	29.9 ± 5.2	SPT-S J223825-5114.3	61.1 ± 12.3	13.71
			SPT-S J223553-5131.8	21.3 ± 4.5	17.52
136	4FGL J2117.1-5307*	29.7 ± 4.4	SPT-S J211704-5306.8	3.3 ± 1.3	0.80
			SPT-S J211701-5306.7	7.0 ± 1.8	1.12
137	4FGL J0231.2-5754	29.6 ± 4.2	SPT-S J023108-5755.1	52.6 ± 10.6	0.98
138	4FGL J2100.0-4356*	29.6 ± 4.8	L	L	L
139	4FGL J2017.5-4113	29.6 ± 4.8	SPT-S J201729-4115.3	16.4 ± 3.5	1.56
140	4FGL J0622.4-6433	29.4 ± 5.4	SPT-S J062307-6436.4	357.7 ± 71.7	5.25
			SPT-S J062336-6434.6	14.3 ± 3.1	7.46
			SPT-S J062020-6438.8	13.7 ± 3.0	14.63
141	4FGL J2001.9-5737	29.0 ± 4.4	SPT-S J200204-5736.6	6.2 ± 1.6	1.47
142	4FGL J0014.1-5022	28.8 ± 4.2	FSPT-S J001411-5022.5	1.8 ± 0.4	0.33
143	4FGL J2159.6-4620*	28.8 ± 5.0	L	L	L
144	4FGL J0156.8-4744	28.7 ± 4.1	SPT-S J015645-4744.2	7.5 ± 1.9	1.01
145	4FGL J2313.9-4501	28.7 ± 5.9	SPT-S J231408-4455.8	78.0 ± 15.7	5.71
146	4FGL J0251.5-5958	28.7 ± 4.0	SPT-S J025125-6000.1	156.6 ± 31.4	2.10
			SPT-S J025202-5953.6	4.8 ± 1.4	5.84
147	4FGL J2326.9-4130*	28.3 ± 7.2	SPT-S J232625-4140.2	43.9 ± 8.9	11.35
			FSPT-S J232719-4134.5	3.1 ± 0.6	5.80
148	4FGL J0626.4-4259	28.2 ± 4.8	FSPT-S J062636-4258.1	3.7 ± 0.8	2.07
149	4FGL J0657.4-4658*	27.8 ± 4.7	L	L	L
150	4FGL J0445.1-6012	27.6 ± 3.9	SPT-S J044500-6014.9	16.5 ± 3.5	2.43
151	4FGL J2234.2-4156*	26.8 ± 3.9	SPT-S J223415-4156.9	9.7 ± 2.3	0.49
152	4FGL J2024.8-6459	26.7 ± 4.5	SPT-S J202445-6458.6	95.2 ± 19.1	0.83
153	4FGL J2115.6-4938	26.4 ± 4.2	SPT-S J211545-4938.8	6.9 ± 1.8	1.46
154	4FGL J0646.4-5455	26.3 ± 3.2	SPT-S J064628-5451.2	27.7 ± 5.7	4.17
155	4FGL J0503.1-6045	26.2 ± 6.6	SPT-S J050401-6049.8	59.6 ± 12.0	7.70
			SPT-S J050335-6058.4	10.0 ± 2.4	13.67
156	4FGL J2041.1-6138*	26.1 ± 4.3	SPT-S J204111-6139.8	16.2 ± 3.4	1.73
157	4FGL J0328.4-4736*	25.4 ± 3.7	SPT-S J032842-4739.6	9.1 ± 2.2	4.12
158	4FGL J0651.9-4330*	25.0 ± 5.5	L	L	L
159	4FGL J0048.6-6347*	25.0 ± 3.7	L	L	L
160	4FGL J2046.8-4258	25.0 ± 4.5	SPT-S J204644-4257.2	7.7 ± 2.0	1.82
			SPT-S J204643-4256.7	3.6 ± 1.5	2.13
161	4FGL J0442.0-5432*	24.9 ± 3.9	SPT-S J044230-5431.7	52.3 ± 10.5	4.15
162	4FGL J0416.2-4353	24.9 ± 4.1	SPT-S J041613-4350.9	9.8 ± 2.3	2.44
			SPT-S J041642-4401.9	7.6 ± 1.9	9.81
163	4FGL J2040.1-4621	24.6 ± 4.7	FSPT-S J204006-4620.3	4.6 ± 0.9	1.69
164	4FGL J0437.4-6155	24.5 ± 3.6	SPT-S J043718-6157.0	5.9 ± 1.6	1.33
165	4FGL J0026.6-4600	24.3 ± 3.9	SPT-S J002636-4601.1	8.9 ± 2.2	0.19

Table 2
(Continued)

Index	4FGL Name	$S_{0.1-100GeV}$ (10^{-13} erg cm^{-2} s^{-1})	SPT Name	S_{150GHz} (mJy)	dr_1 (arcmin)
166	4FGL J0009.8-4317	24.3 ± 3.7	SPT-S J000949-4316.7	18.2 ± 3.8	1.14
167	4FGL J0017.1-4605*	24.2 ± 4.1	L	L	L
168	4FGL J2105.2-5143	24.2 ± 4.7	SPT-S J210524-5145.7	26.6 ± 5.5	2.36
169	4FGL J0225.5-5530*	24.1 ± 11.7	FSPT-S J022532-5528.6	4.0 ± 0.8	1.68
170	4FGL J0654.6-4952	24.1 ± 4.6	SPT-S J065519-4951.9	38.5 ± 7.8	6.30
171	4FGL J0019.2-5640	24.1 ± 3.5	SPT-S J001926-5641.7	79.4 ± 16.0	1.85
172	4FGL J2353.1-4806	23.9 ± 3.7	SPT-S J235311-4806.0	62.0 ± 12.5	0.68
173	4FGL J0550.5-4356*	23.9 ± 4.3	FSPT-S J055026-4356.9	4.8 ± 1.0	0.87
174	4FGL J2209.8-5028	23.8 ± 4.5	SPT-S J221040-5026.9	98.5 ± 19.8	7.55
			SPT-S J221015-5031.1	25.4 ± 5.3	4.58
175	4FGL J0357.6-4625	23.4 ± 3.5	SPT-S J035728-4625.6	69.1 ± 13.9	1.98
176	4FGL J0533.3-5549	23.3 ± 4.8	SPT-S J053324-5549.5	57.8 ± 11.6	0.76
177	4FGL J0343.3-6303*	23.2 ± 3.8	SPT-S J034325-6303.3	8.4 ± 2.0	0.30
178	4FGL J0131.7-5346*	23.2 ± 3.8	L	L	L
179	4FGL J0140.5-4730*	23.1 ± 4.5	SPT-S J013940-4732.0	48.8 ± 9.9	8.94
			SPT-S J014046-4725.7	5.9 ± 1.6	5.12
180	4FGL J0009.1-5012*	23.0 ± 4.0	SPT-S J000835-5009.6	13.7 ± 3.0	6.36
181	4FGL J2249.7-5944	22.9 ± 3.8	SPT-S J224938-5944.2	6.2 ± 1.7	0.69
182	4FGL J0624.7-4903*	22.9 ± 4.5	FSPT-S J062358-4904.1	3.6 ± 0.7	8.08
183	4FGL J0110.0-4019	22.8 ± 4.3	SPT-S J010956-4020.7	12.3 ± 2.8	2.23
184	4FGL J2029.5-4237*	22.7 ± 2.8	L	L	L
185	4FGL J0035.0-5728	22.7 ± 4.0	SPT-S J003504-5726.2	17.5 ± 3.7	2.07
186	4FGL J0225.6-4502	22.5 ± 5.4	SPT-S J022544-4503.2	355.8 ± 71.3	1.65
187	4FGL J2107.6-4148	22.5 ± 4.5	SPT-S J210723-4145.5	23.8 ± 4.9	4.39
188	4FGL J0102.6-5639	22.5 ± 4.5	SPT-S J010210-5637.2	120.3 ± 24.1	4.32
			SPT-S J010303-5639.3	5.9 ± 1.7	3.57
189	4FGL J0049.6-4500	22.3 ± 3.8	SPT-S J004916-4457.1	1158.0 ± 232.0	5.35
190	4FGL J0358.1-5954	22.2 ± 3.5	SPT-S J035814-5952.3	21.4 ± 4.4	2.18
191	4FGL J0056.6-5317	22.1 ± 3.5	SPT-S J005621-5318.6	20.3 ± 4.3	2.65
192	4FGL J0440.3-4333	22.0 ± 5.5	SPT-S J044017-4333.0	161.5 ± 32.4	0.77
			SPT-S J044117-4313.6	111.3 ± 22.3	22.05
193	4FGL J0623.9-5259	22.0 ± 4.1	SPT-S J062337-5258.3	7.9 ± 2.0	3.07
			SPT-S J062337-5257.8	3.3 ± 1.3	3.32
194	4FGL J0414.7-4300*	22.0 ± 2.7	L	L	L
195	4FGL J0604.5-4851	21.8 ± 4.7	SPT-S J060433-4849.6	155.4 ± 31.2	1.83
196	4FGL J0647.0-5138	21.8 ± 4.3	SPT-S J064709-5135.8	9.4 ± 2.3	2.54
197	4FGL J0004.4-4001*	21.8 ± 4.4	SPT-S J000433-4000.5	19.1 ± 4.0	1.33
			SPT-S J000444-4007.3	0.7 ± 1.5	6.58
198	4FGL J0601.4-6057*	21.6 ± 4.4	L	L	L
199	4FGL J0500.6-4911	21.5 ± 4.0	SPT-S J050037-4912.1	15.5 ± 3.3	1.22
200	4FGL J0658.1-5840	21.2 ± 4.1	SPT-S J065814-5840.3	123.9 ± 24.9	0.69
201	4FGL J2357.0-4840	21.1 ± 3.7	SPT-S J235721-4838.3	111.7 ± 22.4	3.51
202	4FGL J2247.7-5857*	20.8 ± 4.5	FSPT-S J224745-5854.9	4.1 ± 0.8	2.44
203	4FGL J0127.4-4813	20.6 ± 3.4	SPT-S J012715-4813.4	127.5 ± 25.6	2.27
204	4FGL J0025.4-4838*	20.5 ± 3.9	L	L	L
205	4FGL J2031.2-4121	20.5 ± 4.2	SPT-S J203055-4117.1	35.9 ± 7.3	5.63
206	4FGL J0438.2-4243*	20.4 ± 4.4	SPT-S J043831-4240.0	5.8 ± 1.6	4.72

Table 2
(Continued)

Index	4FGL Name	$S_{0.1-100GeV}$ (10^{-13} erg cm^{-2} s^{-1})	SPT Name	S_{150GHz} (mJy)	dr_1 (arcmin)
207	4FGL J2246.7-5207	20.4 ± 4.3	FSPT-S J224642-5206.6	4.4 ± 0.9	0.91
208	4FGL J0245.4-5950	20.4 ± 3.7	SPT-S J024452-5947.9	29.3 ± 6.0	4.49
209	4FGL J2151.2-4034*	20.3 ± 4.1	L	L	L
210	4FGL J2240.7-4746	20.1 ± 3.6	SPT-S J224043-4747.3	10.1 ± 2.4	0.96
211	4FGL J0047.1-6203	20.1 ± 4.1	SPT-S J004750-6206.7	5.5 ± 1.5	6.30
212	4FGL J0622.7-4141	20.0 ± 3.2	L	L	L
213	4FGL J0119.4-5354	19.8 ± 3.6	SPT-S J011950-5357.2	189.4 ± 38.0	3.98
214	4FGL J2332.1-4118	19.8 ± 4.5	SPT-S J233218-4118.6	113.7 ± 22.8	2.44
215	4FGL J0541.1-4854	19.5 ± 3.9	L	L	L
216	4FGL J0553.9-5048*	19.4 ± 3.7	FSPT-S J055359-5051.7	3.4 ± 0.7	2.97
217	4FGL J0650.2-5144*	19.3 ± 4.1	SPT-S J065009-5144.5	7.7 ± 2.0	1.13
218	4FGL J0206.8-5744	19.2 ± 3.4	SPT-S J020641-5749.7	6.4 ± 1.7	4.97
			SPT-S J020721-5751.3	3.5 ± 1.2	7.73
219	4FGL J0420.3-6016	19.2 ± 3.3	L	L	L
220	4FGL J0159.3-4523	19.2 ± 5.5	SPT-S J015906-4515.6	42.2 ± 8.6	7.69
221	4FGL J0550.3-5733	19.0 ± 4.3	SPT-S J055009-5732.4	542.9 ± 108.8	1.68
222	4FGL J2355.2-5247*	18.8 ± 4.0	L	L	L
223	4FGL J0414.8-5338	18.6 ± 4.4	FSPT-S J041458-5339.7	4.0 ± 0.8	1.43
224	4FGL J0406.0-5407	18.5 ± 3.7	SPT-S J040608-5404.7	8.6 ± 2.0	2.73
225	4FGL J2321.9-4842*	18.3 ± 4.2	SPT-S J232216-4836.2	7.7 ± 2.0	6.83
226	4FGL J2012.1-5234*	17.9 ± 4.3	SPT-S J201213-5232.8	7.3 ± 1.9	1.54
			SPT-S J201142-5235.2	24.8 ± 5.1	4.16
227	4FGL J2213.5-4754	17.9 ± 3.8	SPT-S J221330-4754.4	8.5 ± 2.1	0.44
228	4FGL J0214.8-6150	17.7 ± 3.8	SPT-S J021415-6149.5	385.3 ± 77.2	3.99
229	4FGL J0350.4-5144	17.0 ± 3.5	FSPT-S J035028-5144.7	4.1 ± 0.8	0.20
230	4FGL J0150.6-5448	17.0 ± 3.3	SPT-S J015044-5450.1	10.2 ± 2.3	2.02
231	4FGL J0443.4-4152	17.0 ± 3.6	SPT-S J044328-4151.6	6.1 ± 1.7	1.41
232	4FGL J2046.9-5409*	16.9 ± 4.0	FSPT-S J204701-5412.7	3.8 ± 0.8	2.96
233	4FGL J0003.3-5905	16.8 ± 3.4	SPT-S J000312-5905.7	12.6 ± 2.7	1.37
234	4FGL J0125.9-6303*	16.6 ± 3.4	FSPT-S J012541-6305.7	2.2 ± 0.4	3.11
			FSPT-S J012547-6302.7	6.1 ± 1.2	1.53
235	4FGL J0539.2-6333*	16.6 ± 3.7	L	L	L
236	4FGL J0654.0-4152	16.4 ± 4.5	SPT-S J065400-4151.8	28.6 ± 5.9	1.25
237	4FGL J0301.6-5617*	16.2 ± 3.3	FSPT-S J030115-5616.7	3.5 ± 0.7	3.57
238	4FGL J0652.1-4813	16.0 ± 3.9	SPT-S J065203-4809.0	6.2 ± 1.7	4.33
239	4FGL J2030.3-5038*	16.0 ± 3.9	L	L	L
240	4FGL J0056.6-4452	15.8 ± 3.6	SPT-S J005646-4451.0	91.8 ± 18.4	2.10
241	4FGL J0407.7-5702*	15.7 ± 3.6	L	L	L
242	4FGL J0314.4-4805*	15.7 ± 3.3	SPT-S J031428-4807.8	10.1 ± 2.4	2.76
243	4FGL J0031.5-5648*	15.4 ± 3.6	FSPT-S J003136-5646.6	2.3 ± 0.5	1.80
244	4FGL J0429.3-4326	15.3 ± 3.5	SPT-S J042924-4328.5	15.2 ± 3.3	1.98
245	4FGL J0309.4-4000	15.0 ± 3.4	SPT-S J030912-4001.8	27.8 ± 5.7	3.07
246	4FGL J0049.5-4150	14.8 ± 3.6	SPT-S J004939-4151.3	4.0 ± 1.6	1.06
247	4FGL J2343.0-4756*	14.8 ± 2.7	FSPT-S J234302-4757.8	5.5 ± 1.1	1.07
248	4FGL J0610.8-4911*	14.7 ± 3.8	L	L	L
249	4FGL J2311.6-4427*	14.6 ± 3.8	L	L	L
250	4FGL J0102.0-6240*	14.4 ± 3.3	FSPT-S J010147-6243.1	3.9 ± 0.8	2.73

Table 2
(Continued)

Index	4FGL Name	$S_{0.1-100GeV}$ (10^{-13} erg cm^{-2} s^{-1})	SPT Name	S_{150GHz} (mJy)	dr_1 (arcmin)
251	4FGL J0611.4-4722*	14.3 ± 3.7	L	L	L
252	4FGL J2042.1-5320*	14.2 ± 3.9	FSPT-S J204217-5321.1	2.3 ± 0.5	1.62
			FSPT-S J204220-5326.9	4.7 ± 0.9	6.96
253	4FGL J0401.0-5353	14.1 ± 3.6	L	L	L
254	4FGL J2127.6-5959	13.7 ± 3.2	SPT-S J212722-6000.8	12.9 ± 2.8	2.80
255	4FGL J2316.9-5210	13.6 ± 3.3	SPT-S J231702-5210.0	8.2 ± 1.9	0.55
256	4FGL J2042.7-5415	13.6 ± 2.2	FSPT-S J204304-5411.6	2.1 ± 0.4	4.89
257	4FGL J2239.2-5657	13.6 ± 3.3	SPT-S J223911-5701.0	520.7 ± 104.3	3.95
258	4FGL J2202.7-5637	13.4 ± 3.4	SPT-S J220253-5635.7	40.5 ± 8.2	2.30
259	4FGL J0246.0-4838*	13.4 ± 4.1	L	L	L
260	4FGL J0459.7-5413*	13.3 ± 3.2	L	L	L
261	4FGL J0023.6-4209*	13.3 ± 3.3	SPT-S J002443-4202.2	12.6 ± 2.8	14.13
			SPT-S J002401-4200.9	8.6 ± 2.1	9.63
			SPT-S J002300-4206.4	8.0 ± 2.0	7.63
262	4FGL J0311.5-4402	13.2 ± 3.2	FSPT-S J031103-4402.5	1.8 ± 0.4	5.08
263	4FGL J0214.4-5822	12.9 ± 3.1	SPT-S J021409-5822.0	46.5 ± 9.4	1.95
264	4FGL J0450.7-4938	12.8 ± 3.2	SPT-S J045101-4936.3	80.8 ± 16.2	3.76
265	4FGL J0331.1-5243	12.4 ± 3.1	SPT-S J033113-5241.7	27.2 ± 5.6	2.27
			SPT-S J033124-5258.4	118.9 ± 23.8	14.64
266	4FGL J2321.0-6308	12.3 ± 3.0	SPT-S J232042-6309.7	3.0 ± 1.5	2.62
267	4FGL J0328.8-5715	12.1 ± 3.4	L	L	L
268	4FGL J0316.0-5626	11.8 ± 2.9	L	L	L
269	4FGL J0058.3-4603*	11.4 ± 3.1	L	L	L
270	4FGL J0640.9-5204*	11.4 ± 3.3	SPT-S J064110-5202.5	24.4 ± 5.1	2.62
271	4FGL J0106.9-4832	11.0 ± 2.7	SPT-S J010655-4831.4	27.3 ± 5.6	0.78
272	4FGL J0118.3-6008*	11.0 ± 2.8	SPT-S J011823-6007.8	10.8 ± 2.5	0.82
273	4FGL J0347.0-6400*	9.8 ± 1.8	L	L	L
274	4FGL J0133.2-4533	9.7 ± 3.0	FSPT-S J013309-4535.4	1.5 ± 0.3	1.95
275	4FGL J0215.0-5330*	9.7 ± 2.9	FSPT-S J021515-5328.7	4.3 ± 0.9	2.30
276	4FGL J0338.7-5706	9.4 ± 3.0	L	L	L
277	4FGL J0101.7-5455	9.3 ± 2.9	FSPT-S J010141-5455.8	4.7 ± 0.9	0.79
278	4FGL J0620.7-5034*	9.2 ± 3.0	SPT-S J062045-5033.9	8.0 ± 2.0	0.47
279	4FGL J0317.8-4414	8.5 ± 3.1	SPT-S J031757-4414.0	74.7 ± 15.0	0.82
280	4FGL J0201.1-4347	8.1 ± 3.0	FSPT-S J020110-4346.8	4.4 ± 0.9	1.00
281	4FGL J0308.9-4702*	6.9 ± 2.7	FSPT-S J030858-4700.5	1.5 ± 0.3	1.92

(This table is available in machine-readable form.)

Appendix B
Full 4FGL Multiwavelength Association Table

The full 4FGL multiwavelength association table is available online.[9] We display an example table of the first five rows as shown in Table 3. Note that the index and table format are consistent with Table 2. Additionally, the source name of the multiwavelength counterpart (SUMSS/SPT/WISE/RASS) starting with "*" represents that the source satisfies the selection criteria described in Section 3.2. For each association, multiple counterparts are ranked based on the p-value from low to high. We attach an example table for illustration. The column description and units are listed below.

1. 4FGL Name: 4FGL source name
2. SPT Name: SPT source name
3. SPT RA: SPT R.A.(J2000) in degrees
4. SPT DEC: SPT decl(J2000) in degrees
5. S_{95}: (Deboosted) flux in 95 GHz in mJy
6. S_{150}: (Deboosted) flux in 150 GHz in mJy
7. S_{220}: (Deboosted) flux in 220 GHz in mJy
8. Redshift: Measured redshift if available in NED
9. RASS name: RASS source name
10. SUMSS name: SUMSS source name
11. WISE name: AllWISE source name

[9] https://github.com/lizhong-phys/4FGL-SPT.git

Table 3
Example Table of Full 4FGL Multiwavelength Association

Index	4FGL Name (4FGL*)	SPT Name (SPT-S*)	SPT R.A. (deg)	SPT decl. (deg)	S_{95GHz} (mJy)	S_{150GHz} (mJy)	S_{220GHz} (mJy)	z	RASS Name (RASS*)	SUM (S
0	J0538.8−4405	J053850−4405.1	84.710495	−44.085197	5958.9	4843.0	3905.6	0.89400	J053850.2−440504	J053
		L	L	L	L	L	L	L	L	J053
1	J2329.3−4955	J232920−4955.6	352.33704	−49.927555	1064.1	522.1	426.4	0.51800	L	J232
2	J0449.4−4350	J044924−4350.0	72.351730	−43.833607	127.9	119.3	108.7	0.10700	J044924.2−435002	J044
3	J2056.2−4714	J205616−4714.8	314.06787	−47.247147	1769.5	1424.9	1199.5	1.48900	J205615.8−471446	J205
4	J0210.7−5101	J021045−5101.0	32.689522	−51.017540	1868.2	1504.4	1196.5	0.99900	J021046.8−510055	J021
		L	L	L	L	L	L	L	L	J021
5	J0532.0−4827	J053158−4827.6	82.994888	−48.461178	450.9	400.3	353.0	L	J053159.9−482751	J053

Note. Full table in multiple file formats can be found in https://github.com/lizhong-phys/4FGL-SPT.git.

(This table is available in its entirety in machine-readable form.)

Appendix C
Thumbnails

We make the thumbnails of all 282 4FGL sources within the 2500 deg^2 SPT-SZ survey field as shown in Figure 12, similar to Figure 3. The index is consistent with Table 2, where the 282 4FGL sources are sorted by γ-ray flux. The thumbnails are attached below and can also be downloaded via https://github.com/lizhong-phys/4FGL-SPT.git. Each 0°. 7 × 0°. 7 thumbnail in the gray background is the high-pass-filtered SPT 150 GHz image. The SPT images appear to be ringing because of the high-pass point-source filter. The blue ellipse at the center is the 4FGL 95% (2σ) uncertainty region, and the blue dashed ellipse represents the 4σ 4FGL beam. The green diamond marks the position of SPT-SZ sources at ≥4.5σ from Everett et al. (2020). The red contours are derived from the 843 MHz SUMSS map in units of 3σ, 4σ, 5σ, 7σ, 10σ, 15σ, 20σ, and 25σ. Each radio detection in the SUMSS catalog is also marked by a red dot for the cases too faint to be seen in contours. The

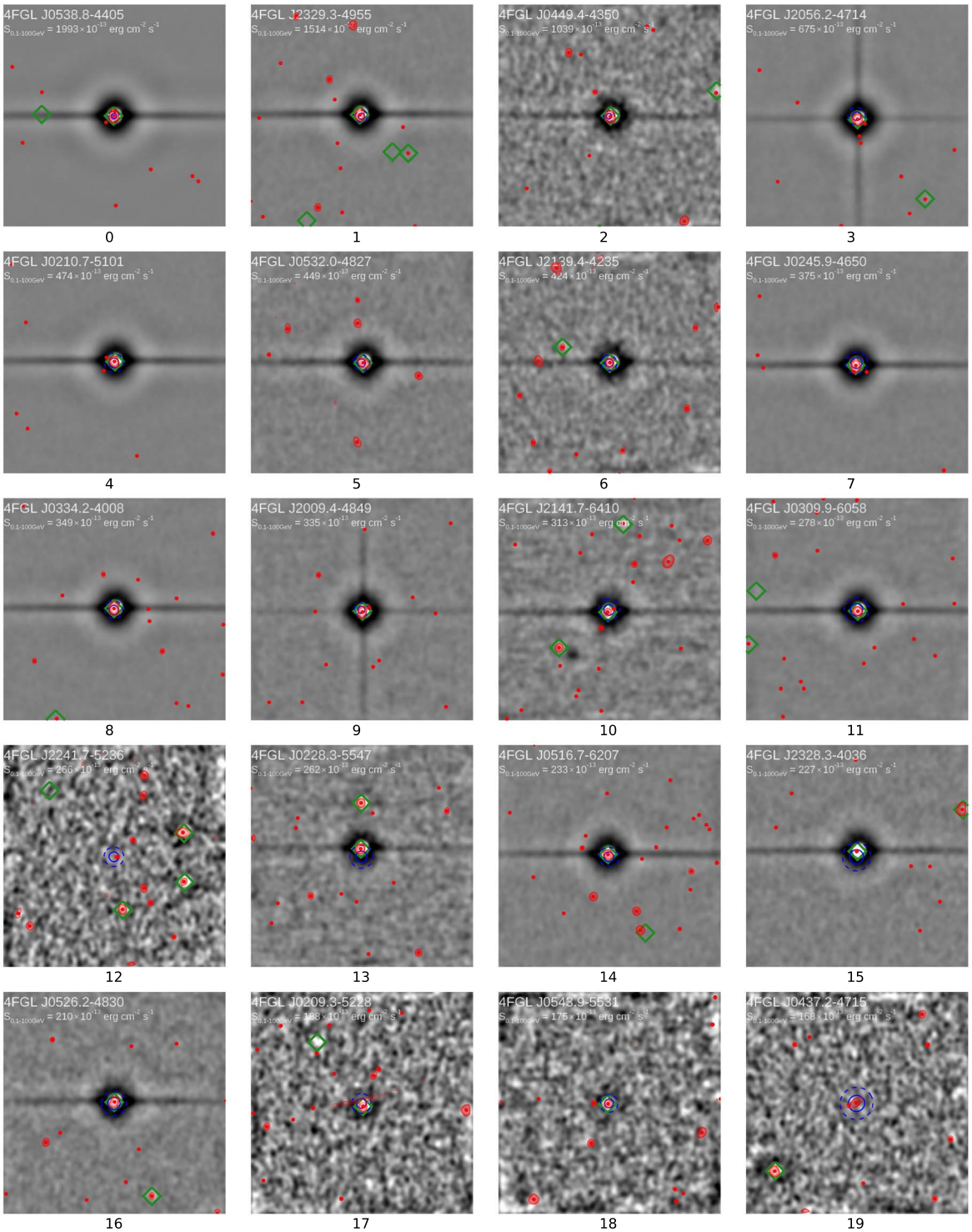

Figure 12. SPT thumbnails of 282 4FGL sources. The full version can also be downloaded at https://github.com/lizhong-phys/4FGL-SPT.git. (The complete figure set (15 images) is available.)

4FGL source name is in the upper left corner, as well as the γ-ray energy flux.

ORCID iDs

Lizhong Zhang (张力中) https://orcid.org/0000-0003-0232-0879
Joaquin D.Vieira https://orcid.org/0000-0001-7192-3871
Marco Ajello https://orcid.org/0000-0002-6584-1703
Matthew A. Malkan https://orcid.org/0000-0001-6919-1237
Melanie A. Archipley https://orcid.org/0000-0002-0517-9842
Joseph Capota https://orcid.org/0000-0002-8491-3012
Allen Foster https://orcid.org/0000-0002-7145-1824

References

Abazajian, K. N., Adshead, P., Ahmed, Z., et al. 2016, arXiv:1610.02743
Abdollahi, S., Acero, F., Ackermann, M., et al. 2020, ApJS, 247, 33
Ajello, M., Gasparrini, D., Sánchez-Conde, M., et al. 2015, ApJL, 800, L27
Atwood, W. B., Abdo, A. A., Ackermann, M., et al. 2009, ApJ, 697, 1071
Benson, B. A., Ade, P. A. R., Ahmed, Z., et al. 2014, Proc. SPIE, 9153, 91531P
Biggs, A. D., Ivison, R. J., Ibar, E., et al. 2011, MNRAS, 413, 2314
Blandford, R., Meier, D., & Readhead, A. 2019, ARA&A, 57, 467
Browne, I. W. A., & Cohen, A. M. 1978, MNRAS, 182, 181
Carlstrom, J. E., Ade, P. A. R., Aird, K. A., et al. 2011, PASP, 123, 568
Cutri, R. M., Wright, E. L., Conrow, T., et al. 2013, VizieR On-line Data Catalog: II/328
D'Abrusco, R., Massaro, F., Ajello, M., et al. 2012, ApJ, 748, 68
Dermer, C. D. 1995, ApJL, 446, L63
Dermer, C. D., & Giebels, B. 2016, CRPhy, 17, 594
Downes, A. J. B., Peacock, J. A., Savage, A., & Carrie, D. R. 1986, MNRAS, 218, 31
Dutka, M. S., Carpenter, B. D., Ojha, R., et al. 2017, ApJ, 835, 182
Everett, W. B., Zhang, L., Crawford, T. M., et al. 2020, ApJ, 900, 55
Funk, S. 2015, ARNPS, 65, 245
Ghisellini, G. 2019, Rendiconti Lincei. Scienze Fisiche e Naturali, 30, 137
Ghisellini, G., Righi, C., Costamante, L., & Tavecchio, F. 2017, MNRAS, 469, 255
Healey, S. E., Romani, R. W., Cotter, G., et al. 2008, ApJS, 175, 97
Ivison, R. J., Greve, T. R., Dunlop, J. S., et al. 2007, MNRAS, 380, 199
Malkan, M. A., & Moore, R. L. 1986, ApJ, 300, 216
Marcha, M. J. M., Browne, I. W. A., Impey, C. D., & Smith, P. S. 1996, MNRAS, 281, 425
Massaro, E., Maselli, A., Leto, C., et al. 2015, Ap&SS, 357, 75
Massaro, F., & D'Abrusco, R. 2016, ApJ, 827, 67
Massaro, F., D'Abrusco, R., Tosti, G., et al. 2012, ApJ, 750, 138
Mauch, T., Murphy, T., Buttery, H. J., et al. 2003, MNRAS, 342, 1117
Meyer, M., Scargle, J. D., & Blandford, R. D. 2019, ApJ, 877, 39
Paliya, V. S., Marcotulli, L., Ajello, M., et al. 2017, ApJ, 851, 33
Perlman, E. S., Madejski, G., Georganopoulos, M., et al. 2005, ApJ, 625, 727
Pushkarev, A. B., Kovalev, Y. Y., Lister, M. L., & Savolainen, T. 2009, A&A, 507, L33
Schinzel, F. K., Petrov, L., Taylor, G. B., et al. 2015, ApJS, 217, 4
Schinzel, F. K., Petrov, L., Taylor, G. B., & Edwards, P. G. 2017, ApJ, 838, 139
Stickel, M., Padovani, P., Urry, C. M., Fried, J. W., & Kuehr, H. 1991, ApJ, 374, 431
Stocke, J. T., Morris, S. L., Gioia, I. M., et al. 1991, ApJS, 76, 813
Urry, C. M., & Padovani, P. 1995, PASP, 107, 803
Vieira, J. D., Crawford, T. M., Switzer, E. R., et al. 2010, ApJ, 719, 763
Voges, W., Aschenbach, B., Boller, T., et al. 1999, A&A, 349, 389
Voges, W., Aschenbach, B., Boller, T., et al. 2000, VizieR On-line Data Catalog: IX/29
Wright, E. L., Eisenhardt, P. R. M., Mainzer, A. K., et al. 2010, AJ, 140, 1868